FACULTY
OF SCIENCE

LUND
UNIVERSITY

Bose-Einstein Condensate Jets from Different Traps

Emmanuel-Roosevelt D Costa

Thesis submitted for degree of Master of Science
Project duration: 9 months, 60 hp

Supervised by Stephanie Reimann and Philipp Stürmer

Abstract

This thesis presents a numerical study of the emission of jets by a trapped Bose-Einstein Condensate (BEC). The Gross-Pitaevskii equation is used for simulation of this phenomenon. When the scattering length of a trapped BEC is periodically modulated it emits jets of matter. We study how the pattern of these emitted jets changes when a BEC is trapped in a circular trap, an equilateral triangular trap, a square trap and a rectangular trap. Furthermore, we look for correlations between emitted jets and the build-up of waves in the BEC before the emission of jets. The main results from the thesis are, for a BEC trapped in a circle there is a correlation between emitted jets and the build-up of waves in the BEC before the emission of jets. But this correlation does not hold for BECs in polygon-shaped traps.

Acknowledgements

Acronyms

BEC Bose-Einstein Condensate

GPe Gross-Pitaevskii equation

Contents

Chapter 1

Introduction

In the last two decades, the field of ultra-cold gases has become a hot research topic. But its inception can be traced back to almost a hundred years ago. In the early 1920s, S. N. Bose derived a coefficient from Planck's law-which was related to black body radiation-without any assumptions from electrodynamics. Later on, he sent his work to A. Einstein in hopes that it would be translated into German and published. A. Einstein agreed to translate and publish his work [1]. Without knowing, S. N. Bose had used a radical idea that two photons with the same energy were completely indistinguishable. This was a departure from the classical picture that identical particles could be labelled and tracked. A. Einstein, later on, realized this and published two papers to generalize S. N. Bose's ideas and predicted the existence of a Bose-Einstein Condensate (BEC) in 1924 and 1925 [2, 3].

As an ideal monoatomic gas is cooled to 0 K it undergoes Bose-Einstein condensation which is characterized by all atoms being in the same quantum state [4]. When A. Einstein had predicted the existence of BEC he had assumed that there was no interaction between the particles. This often is not the case in reality as atoms usually interact with each other.

Following the initial theoretical prediction of BECs, a large amount of effort was placed into furthering its theoretical description. During the 1960s, E. P. Gross and L. P. Pitaevskii independently arrived at an equation that modelled the dynamics of a BEC when atoms were weakly interacting with each other [5, 6]. The equation today is known as the Gross-Pitaevskii equation (GPe). At that time, it was not known whether it gave realistic predictions since no BECs had been experimentally found.

It was not until 1995 that BECs were experimentally realized [7, 8]. The reason it took such a long time was that new trapping and cooling methods needed to be developed [9–11]. Since then the field of ultra-cold atomic gases has become a highly pursued research topic. Following the experimental discovery, there have been many agreements between predictions made by the GPe and experiments.

Let us recapitulate some of the interesting phenomena exhibited by BECs: When a large amount of angular momentum is added to a BEC, a grid pattern of vortices may appear [12]. This phenomenon has been extensively studied using the GPe [13–17]. Furthermore,

the appearance of these vortices suggests links to superfluidity [18]. Another phenomenon is that of superradiant Rayleigh scattering where pulses of light are sent into a BEC which then absorbs the light and re-emits it along well-defined directions [19]. In 2015, what is now called a dilute self-bound BEC was theoretically predicted by D. S. Petrov [20]. These dilute self-bound BECs were later experimentally found [21–23]. The droplets densities are much less than air yet liquid droplets still form. This goes against predictions of classical van der Waals theory which predicts that liquid droplets cannot exist at such densities. In addition, these dilute self-bound BECs are predicted to form vortices [24].

Finally, we arrive at the phenomenon that inspired this thesis. In 2017, researchers at Chicago university discovered a new phenomenon exhibited by a BEC [25]. They had shaped a BEC into a two-dimensional disk using lasers and then varied the scattering length between the particles in a sinusoidal pattern. As a result, jets of matter were observed escaping from the trap (like the one shown in figure 1.1). These jets formed an asymmetric pattern. A year later, another group experimentally confirmed the results of [25] and showed phenomenological agreement between the experiment and predictions made by the GPe [26]. One significant result shown from their simulations was that momentum in the system was always conserved and that there was a strong correlation between the direction of the waves that formed in the BEC and the emitted jet pattern. After that, in 2020, theoretical and experimental work was done on how these jets were affected when the BEC was trapped in a circular trap. They showed that these jet patterns were dramatically altered compared to the non-rotating case.

To our best knowledge, no one has studied the emission of jets from polygon-shaped traps. To this end, we are interested in replicating the simulations from [26] and testing how the pattern of the jet changes for polygonal-shaped traps. Furthermore, we would like to see whether the main conclusions from [26] hold for polygonal traps.

The structure of this thesis is as follows. Firstly, we will give a brief introduction to what characterizes a BEC. Then, by using the characteristics of a BEC, the GPe equation will be derived. After that, an in-depth explanation of the algorithm, which is used to get the results, will be given. To better understand the algorithm, an example of a one-dimensional harmonic oscillator will be used. Finally, the algorithm will be generalized to solve the GPe. Then, the main problem of this thesis will be defined and a model for the physical problem will be presented. In the final section of this chapter, by studying the model in a simplified system, a relation for resonating waves will be derived.

The third chapter is dedicated to the results and discussion. The first section of the chapter will replicate the results form [26]. For the remaining section, the results of the polygonal traps will be presented and compared to each other.

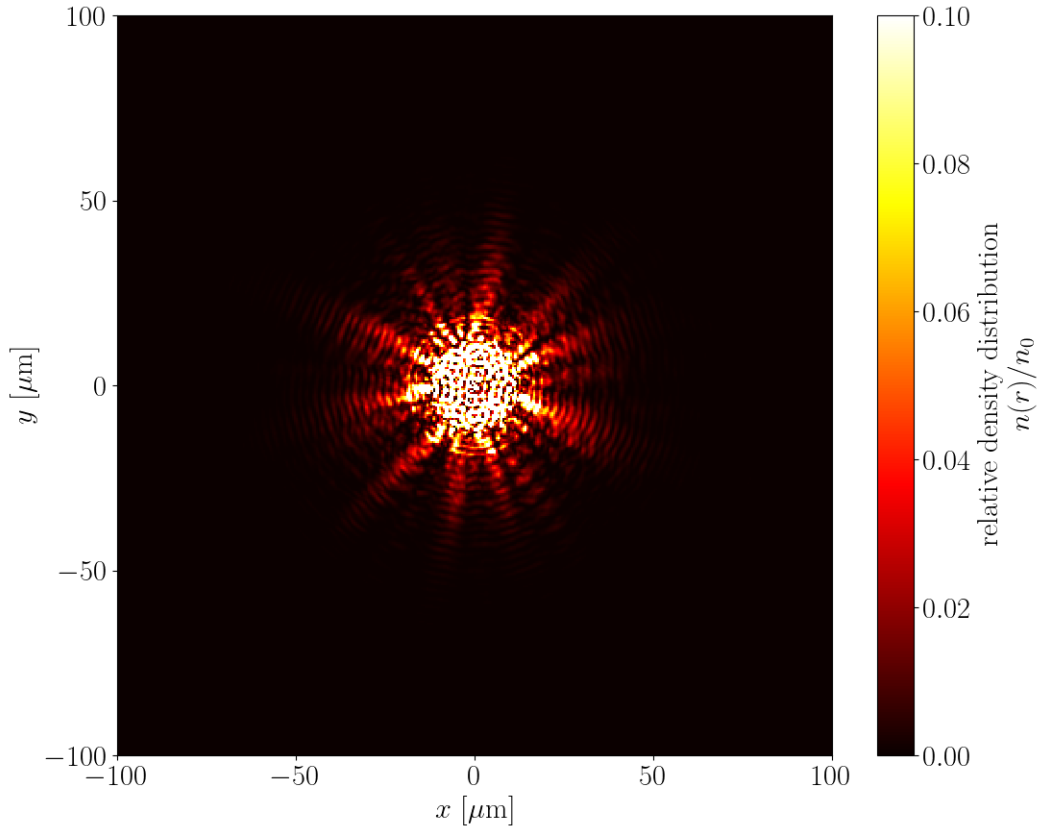Figure 1.1: Shows the relative density distribution $n(\vec{r})/n_0$ of a BEC, where n_0 is average density of the ground state. The plot has been simulated by the GPe and shows the BEC after its scattering length has been periodically varied for 50 ms. Jets which form an asymmetric pattern can be seen escaping the trap. The color bar has a max value of 0.1 because it makes the jets appear clearly.

Chapter 2

Theory

We start this thesis by giving a brief overview of the physics of Bose-Einstein condensation. After that, a Schrödinger-like equation called the Gross-Pitaevskii equation (GPe) will be derived from first principles. The method of solving this equation numerically via imaginary time propagation will be discussed before turning to the central problem for this thesis.

2.1 Bose-Einstein Condensation

To understand what a BEC is some basic results of quantum mechanics must be stated. One result is that bounded systems exhibit discrete energy levels. This is true for N non-interacting particles in a box.

A question to ask is whether all the non-interacting particles can occupy the same energy level. The answer depends on the type of particle. According to QM, a particle can either be a boson or fermion. The difference between the two is related to the spin of the particle: bosons have integer spin and fermions have half-integer spin. In a many body system, bosons with the same spin can occupy the same energy level, there is no restriction. However, for fermions, only particles with different spins can occupy the same energy level. The other fermions are forced to occupy different energy levels [27].

A BEC is a state of matter just like a solid, liquid or gas. To experimentally make a BEC, monoatomic gases of specific atomic species are used [4]. When such a gas is cooled to near 0 K it transitions into a BEC. The difference between a gas and BEC is that all the atoms in a BEC can occupy the same quantum state which means a BEC is made of bosons.

In the next section we derive the Schrödinger-like equation that will help us model the jet emissions due to changing the scattering length of the BEC.

2.2 Deriving the Modelling Equation

A single system may be described by multiple models. For example, Hook's law models the behaviour of how an elastic band stretches when a force is applied to it. However, Hook's

law breaks down when the elastic band is overstretched. This means that Hook's law works well for a certain regime. In this section, a model that describes the dynamics of a BEC in a small regime is derived. Even though this is the case, a wealth of information can be extracted about the system.

In the previous section it was stated that the transition to a BEC occurs at near 0 K. At these temperatures, the atoms in the BEC have low energy. This is the first assumption made for the model. The second assumption is that the atoms are weakly interacting to the extent that all particles can occupy the lowest energy level. In some sense, this is not a realistic approximation because there will always be some fluctuations of particles from the ground state to higher energy levels.

Before starting the derivation, an approximation is found using the second assumption. Consider a state ket $|\Psi\rangle$ that represents a BEC with N particles. Suppose for the moment that the particles in the BEC are non-interacting. Then $|\Psi\rangle$ can be written as [4]

$$|\Psi\rangle = N|\phi_1\rangle \otimes |\phi_2\rangle \otimes |\phi_3\rangle \otimes .... \otimes |\phi_N\rangle = N \bigotimes_{i=1}^{N} |\phi_i\rangle, \tag{2.1}$$

where N is the number of particles, $\otimes$ is the tensor product and $|\phi_i\rangle$ for $1 \leq i \leq N$ are all the same single particle wavefunction but attributed to each individual particle in the system. Equation (2.1) is referred to as the Hartree or mean-field approach and is an exact relation if the particles of the system are non-interacting. To see why this is true, imagine four non-interacting particles trapped in a box. By using the Schrodinger equation the wavefunction for each particle can be found. Since the particles are non-interacting the shape of the wave function only depends on the box in which the particles are trapped. As a result all the wavefunctions for all the particles are the same. However, in the case of a BEC the particles weakly interact with each other. Therefore, eq (2.1) is an approximation and will repeatedly be used in the derivation of the model.

The Hamiltonian of a many-body system will be the starting point of the derivation. The exact Hamiltonian $\hat{\mathcal{H}}$ of an N particle many-body system can be written as [28]

$$\hat{\mathcal{H}} = \sum_{i=1}^{N} \frac{\hat{p_i}^2}{2m} + \hat{V}_{\text{ext}}(\vec{r}) + \frac{1}{2} \sum_{i=1}^{N} \sum_{j \neq i}^{N} \hat{V}(\vec{r}_i - \vec{r}_j), \tag{2.2}$$

where $\hat{p}_i$ is the momentum of the i-th particle, m is the mass of each particle (in this case all the particles have the same mass), $\hat{V}_{\text{ext}}$ is the external potential, $\hat{V}(\vec{r}_i - \vec{r}_j)$ is the exact interaction potential between the i-th and j–th particle. In principle, plugging the Hamiltonian (equation (2.2)) in the Schrödinger equation and numerically solving it is one way to study the system. Unfortunately, this route would need unrealistic computing power, hence approximations are needed. We start by considering the energy of the system. It is written as [29]

$$E(\Psi) = \frac{\langle\Psi|\hat{\mathcal{H}}|\Psi\rangle}{\langle\Psi|\Psi\rangle}, \tag{2.3}$$

where $\langle\Psi|\Psi\rangle$ is the norm and is equal to N. Since majority of the particles in the BEC are in the lowest energy level this becomes a problem of finding the ground state. But to use approximation (2.1) all the particles need to be in the ground state. In addition to that, the state which is found needs to preserve number of particles. Lagrange multipliers can be used to ensure that the $|\Psi\rangle$ that is found preserves the number of particles $\langle\Psi|\Psi\rangle = N$ [4]. Notice the energy $E = E(\Psi)$ is a function that depends on another function Ψ. This means E is a functional. Therefore, the problem is to find the minimum of the functional

$$F(\Psi) = E(\Psi) - \mu N(\Psi), \tag{2.4}$$

where the constant μ is known as the chemical potential and is the Lagrange multiplier [4]. The functional derivative can be used to find the minimum of eq (2.4). The functional $F(\Psi)$ can be split into four different functional terms that correspond to the kinetic energy $J_{\mathrm{KE}}(\Psi)$, the external potential $J_{\mathrm{Ext}}(\Psi)$, the interaction potential $J_{\mathrm{PE}}(\Psi)$ and a term that preserves the norm $J_{\mathrm{norm}}(\Psi)$. In an equation this would look like

$$F(\Psi) = J_{\mathrm{KE}}(\Psi) + J_{\mathrm{Ext}}(\Psi) + J_{\mathrm{PE}}(\Psi) + J_{\mathrm{Norm}}(\Psi) \tag{2.5}$$

Explicitly the kinetic energy term is

$$J_{\mathrm{KE}}(\Psi) = \langle\Psi|\sum_{i=1}^{N}\frac{\hat{p}_i^{\,2}}{2m}|\Psi\rangle \approx \sum_{i=1}^{N}\frac{\hbar^2}{2m}\int \nabla\psi^*(\vec{r}_i)\nabla\psi(\vec{r}_i)d\vec{r}_i.$$

where the approximation (2.1) was used. The constant $\hbar$ is Planck's reduced constant. The functions $\psi(\vec{r}_i)$ is the wavefunction for the i th particle. The external potential term is

$$J_{\mathrm{Ext}}(\Psi) = \langle\Psi|\hat{V}_{\mathrm{ext}}(\vec{r})|\Psi\rangle \approx \sum_{i=1}^{N}\int \psi^*(\vec{r}_i)V_{\mathrm{ext}}(\vec{r})\psi(\vec{r}_i)d\vec{r}_i.$$

The interaction potential term is

$$J_{\mathrm{PE}}(\Psi) = \langle\Psi|\frac{1}{2}\sum_{i=1}^{N}\sum_{j\neq i}^{N}\hat{V}(\vec{r}_i - \vec{r}_j)|\Psi\rangle$$

$$\approx \frac{1}{2}\sum_{i=1}^{N}\sum_{j\neq i}^{N}\int d\vec{r}_i\int d\vec{r}_j\psi^*(\vec{r}_i)\psi^*(\vec{r}_j)V(|\vec{r}_i - \vec{r}_j|)\psi(\vec{r}_i)\psi(\vec{r}_j).$$

Finally the norm term is

$$J_{\mathrm{Norm}}(\Psi) = -\mu\langle\Psi|\Psi\rangle \approx -\mu\prod_{i=1}^{N}\left(\int \psi^*(\vec{r}_i)\psi(\vec{r}_i)d\vec{r}_i\right).$$

If $F(\Psi)$ takes the ground state of the system as input then it will be at its minimum. Thus, taking functional derivative $F(\Psi)$ equals zero. If we take the functional derivative of eq (2.5) (see appendix A for the full procedure) we get the following equation

$$-\frac{\hbar^2}{2m}\nabla^2\psi(\vec{r}) + V_{\text{ext}}(\vec{r})\psi(\vec{r}) + (N-1)\int|\psi(\vec{r'})|^2 V(|\vec{r}-\vec{r'}|)d\vec{r'}\,\psi(\vec{r}) = \mu\psi(\vec{r}). \qquad (2.6)$$

Two further approximation can be made to the integral term in eq (2.6). The term $V(|\vec{r}-\vec{r'}|)$ relates to the interaction potential between two particles. Since weak interactions between particles are assumed, this would mean that particles only feel a force from each other when they are almost touching. Therefore a contact potential can be used. As a result, $V = g\delta(|\vec{r}-\vec{r'}|)$ where g is known as the scattering potential and $\delta(|\vec{r}-\vec{r'}|)$ the Dirac delta function. The next quantity to consider is the $(N-1)$ outside the integral in equation (2.6). If there are a large number of particles $N - 1 \approx N$ giving

$$-\frac{\hbar^2}{2m}\nabla^2\psi(\vec{r}) + V_{\text{ext}}(\vec{r})\psi(\vec{r}) + Ng|\psi(\vec{r})|^2\psi(\vec{r}) = \mu\psi(\vec{r}). \qquad (2.7)$$

Eq (2.7) is known as the time independent Gross-Pitaevskii equation (GPe) and $\psi(\vec{r})$ is called the wavefunction of the BEC. It describes the BEC with all its particles in the ground state.

To study the dynamics of a BEC the time-dependent GPe [4],

$$-i\hbar\frac{\partial\Phi}{\partial t} = -\frac{\hbar^2}{2m}\nabla^2\Phi + V_{\text{ext}}(\vec{r})\Phi + Ng|\Phi|^2\Phi, \qquad (2.8)$$

can be used.

2.3 Pseudo-Second Order Spectral Algorithm to Solve the GPe

To study the dynamics of a BEC we must ensure that we have the correct ground state of the system. To this end, we dedicate this section to explaining the main idea behind the algorithm that solves the problem. First brief motivation behind how one could develop the an algorithm to find the ground state of a quantum system. After that, the algorithm used in this thesis will be discussed by looking at the 1D harmonic oscillator. Then, the algorithm will be generalized to solving the GPe equation.

2.3.1 Finding the Ground State

In theory, if a guess of a state ket $|\psi\rangle$ is made then by using the imaginary time evolution operator the ground state of the system can be found [30]:

$$\lim_{\tau\to\infty}\exp(-\tau\frac{\mathcal{H}}{\hbar})|\psi\rangle \propto |\phi_0\rangle \qquad (2.9)$$

where $\hat{\mathcal{H}}$ is the Hamiltonian of the system and $|\phi_0\rangle$ is the ground state ket. In practice, Hamiltonians are complicated, therefore numerical methods are needed to solve such problems

Suppose a Hamiltonian has form

$$\mathcal{H} = \frac{p^2}{2m} + V(x).$$

where p is the momentum operator and $V(x)$ is some potential. The method used in this thesis decomposes the imaginary time evolution operator as

$$\exp(-\tau \frac{\mathcal{H}}{\hbar}) = A(x,\tau)B(p,\tau)C(x,\tau) \tag{2.10}$$

where $A(x,\tau)$ and $C(x,\tau)$ are operators that only depend on x meaning they can be represented by a diagonal matrix in position basis. Similarly, $B(p,\tau)$ is an operator that only depends on momentum therefore it can be represented by a diagonal matrix in momentum space. This is advantageous numerically since one could evolve a state $\psi(x)$ in the following procedure

1. Take $\psi(x)$ and compute $C(x,\tau)\psi(x)$

2. Take the new $\psi(x)$ and Fourier transform to $\psi(p)$ then compute $B(p,\tau)\psi(p)$

3. Take $\psi(p)$ and inverse Fourier transform back to $\psi(x)$ then compute $A(x,\tau)\psi$

2.3.2   1D Harmonic Oscillator

It is instructive to see how the algorithm works for simple problems such as the 1D harmonic oscillator before looking at more complicated problems. The Hamiltonian of a 1D harmonic oscillator is given by (mass m and $\hbar$ have been set to 1).

$$\hat{\mathcal{H}} = \hat{T} + \hat{V} = \frac{1}{2}\hat{p}^2 + \frac{1}{2}\omega^2\hat{x}^2. \tag{2.11}$$

The imaginary time evolution operator can be exactly rewritten in the case of the one-dimensional harmonic oscillator as [31]

$$e^{-\tau \frac{\hat{\mathcal{H}}}{\hbar}} = e^{-\tau(\hat{T}+\hat{V})} = e^{-\tau C_V \hat{V}} e^{-\tau C_T \hat{T}} e^{-\tau C_V \hat{V}}, \tag{2.12}$$

where C_V and C_T are functions of imaginary time τ. Notice how similar eqs (2.10) and (2.12) are in their dependence on position x and momentum p. Explicitly C_V and C_T are [31]

$$C_V = \frac{\cosh(\omega\tau) - 1}{\omega\tau \sinh(\omega\tau)}, \quad C_T = \frac{\sinh(\omega\tau)}{\omega\tau}. \tag{2.13}$$

At this point the algorithm described in the previous section can be used to compute the ground state. However, in general, exact decompositions of the imaginary time evolution operator cannot be found. In these cases 2nd, 4th or higher order approximate decomposition of the imaginary time evolution operator are used. Therefore, it is necessary to use a small time step. It is possible to see how this works with the 1D harmonic oscillator case. Taking the limit of $\tau \to 0$ the functions in equation (2.13) can be Taylor expanded as [31]

$$C_V = \frac{1}{2} - \frac{1}{24}\omega^2\tau^2 + \frac{1}{240}\omega^4\tau^4 + ... \tag{2.14}$$

$$C_T = 1 - \frac{1}{6}\omega^2\tau^2 + \frac{1}{120}\omega^4\tau^4 + ... \tag{2.15}$$

if only the first terms from both the expansions are kept, a second order algorithm is obtained [31]. Replacing C_V and C_T by the first term in their expansion makes the imaginary time evolution operator look like

$$e^{-\tau C_V \hat{V}}e^{-\tau C_T \hat{T}}e^{-\tau C_V \hat{V}} \approx e^{-\tau\frac{1}{2}\hat{V}}e^{-\tau\hat{T}}e^{-\tau\frac{1}{2}\hat{V}}. \tag{2.16}$$

Since $\hat{T}$ and $\hat{V}$ do not commute due to fact that $\hat{p}$ and $\hat{x}$ do not commute in quantum mechanics, the identity $e^{\hat{T}}e^{\hat{V}} = e^{\hat{T}+\hat{V}}$ is not true.

Using eq (2.16) one can find the ground state by iterating over the following equation

$$|\psi(\tau + \Delta\tau)\rangle \approx e^{-\Delta\tau\frac{1}{2}\hat{V}}e^{-\Delta\tau\hat{T}}e^{-\Delta\tau\frac{1}{2}\hat{V}}|\psi(\tau)\rangle \tag{2.17}$$

where $|\psi(\tau)\rangle$ is a discretized wave function at time τ (i.e. initialized on a grid of points) and the imaginary time evolution operator is approximated by equation (2.16). The algorithm for each iteration would then work as follows

1. Take state $\psi(\tau, x)$ and then multiply $\psi(\tau, x)$ by $e^{-\frac{\Delta\tau}{2}V}$.

2. Compute $\psi(\tau, p)$ from $\psi(\tau, x)$ using fast Fourier transforms. Then multiply $\psi(\tau, p)$ by $e^{-\Delta\tau T}$.

3. Compute $\psi(\tau, x)$ from $\psi(\tau, p)$ using fast Fourier transforms. Then multiply $\psi(\tau, x)$ by $e^{-\frac{\Delta\tau}{2}V}$.

The three steps combined results in finding the state at time $\Psi(\tau + \Delta\tau, x)$. To reach to some time τ_1 multiple iterations would be needed.

2.3.3 Algorithm for Rotating Anisotropic Harmonic Trap

In the previous section the algorithm used for finding the ground state was described in terms of a 1D harmonic potential. In this section a rotating anisotropic harmonic oscillator is studied. This is now a 2D problem therefore the algorithm needs to be stated for this case. Once this is done, the exact same algorithm with some changes to the rotating anisotropic harmonic Hamiltonian can be used to solve the GPe in 2D. For the Hamiltonian of the rotating anisotropic harmonic trap, work done in [31] shows that the imaginary time evolution operator can be decomposed exactly. But this involves a lot of algebra that takes focus away from the algorithm. Therefore, only the main points how to proceed is stated.

The rotating anisotropic harmonic Hamiltonian can be written as [31]

$$
\begin{aligned}
\mathcal{H} &= \frac{1}{2}(p_x^2 + p_y^2) + \frac{1}{2}\tilde{\omega}_x^2 x^2 + \frac{1}{2}\tilde{\omega}_y^2 y^2 - \tilde{\Omega}(xp_y - yp_x) \\
&\overset{1}{=} \frac{1}{2}(p_x^2 + p_y^2) + \frac{1}{2}\omega_0^2(1+\delta)^2 x^2 + \frac{1}{2}\omega_0^2(1-\delta)^2 y^2 - \tilde{\Omega}(xp_y - yp_x) \\
&\overset{2}{=} T_1(p_x, y) + T_2(x, p_y) + V_1(x, p_y) + V_2(p_x, y)
\end{aligned}
\tag{2.18}
$$

where $\tilde{\omega}_x$, $\tilde{\omega}_y$ are the frequencies along the x and y direction respectively, $\tilde{\Omega}$ is the rate of rotation of the trap. The equality $\overset{1}{=}$ shows a second way to write the Hamiltonian in terms of a deformation parameter δ. The equality $\overset{2}{=}$ shows that the Hamiltonian can be broken into terms that depend p_x, y or x, p_y. This is useful because the state ψ in a p_x, y representation makes T_1 and V_2 diagonal. The applies for T_2 and V_1 in a x, p_y representation. [31] has shown that the imaginary time evolution operator can be exactly decomposed as

$$
e^{-\tau(T_1+T_2+V_1+V_2)} = e^{-\tau C_V(1)T_1 - \tau C_V(2)V_2} e^{-\tau C_T(1)V_1 - \tau C_T(2)T_2} e^{-\tau C_V(1)T_1 - \tau C_V(2)V_2}.
\tag{2.19}
$$

The exact forms of $C_V(1)$, $C_V(2)$, $C_T(1)$ and $C_T(2)$ are given in [31]. The following algorithm can be used to compute the ground state of the system [31]

- Make an initial guess of discretized wave function $\psi(x, y)$

- Compute $\psi(p_x, y)$ from $\psi(x, y)$ using fast Fourier transforms. Then multiply $\psi(p_x, y)$ by $e^{-\tau C_V(1)T_1 - \tau C_V(2)V_2}$.

- Compute $\psi(x, p_y)$ from $\psi(p_x, y)$. Then multiply $\psi(x, p_y)$ by $e^{-\tau C_T(1)V_1 - \tau C_T(2)T_2}$

- Compute $\psi(p_x, y)$ from $\psi(x, p_y)$. Then multiply $\psi(p_x, y)$ by $e^{-\tau C_V(1)T_1 - \tau C_V(2)V_2}$

- Finally, compute $\psi(x, y)$ from $\psi(p_x, y)$

These four steps consist of one iteration. The next iteration starts with final wavefunction computed from the previous iteration.

2.3.4 Solving The Gross-Pitaevskii Equation

The algorithm for finding the ground state of a rotating anisotropic harmonic oscillator was described in the previous section. With some redefinitons of terms from the previous section the same algorithm can be used to solve the time-indepenent GPe. Start by assuming a BEC is in a rotating anisotropic harmonic oscillator and define $T = T_1 + V_1 + T_2 + V_2$ from the previous section. Then the time independent 2D GPe is

$$
(T + g|\psi|^2)\psi(x, y) = \mu\psi(x, y).
\tag{2.20}
$$

Using the imaginary time evolution operator, the ground state of the system can be found. By setting $V(\tau) = g|\psi(\tau)|^2$ the second order algorithm iteration step becomes [31]

$$
\psi(\Delta\tau) = e^{-(1/2)\Delta\tau V(\Delta\tau)} e^{-\Delta\tau T} e^{-(1/2)\Delta\tau V(0)} \psi(0).
\tag{2.21}
$$

Using the algorithm stated in the previous subsection one can solve for the ground state of the system. It is important to note that the algorithm has been used to solve a rotating harmonic oscillator potential. If a more general trap potential V_{ext} is needed. Then redefine $V(\tau) = g|\psi(\tau)|^2$ as follows [31]

$$V(\tau) = g|\psi(\tau)|^2 - U_{\text{HO}}(x) - U_{\text{HO}}(y) + V_{\text{ext}}(x, y), \qquad (2.22)$$

where $U_{\text{HO}}(x)$ is the harmonic oscillator potential along x direction and $U_{\text{HO}}(y)$ is the harmonic oscillator potential along the y direction. The reason for the minus signs is to remove to the harmonic potential from the Hamiltonian. Therefore, iteration equation (2.21) can still be used to find the ground state of the wavefunction.

The code used in this thesis was borrowed from [32]. Now that the algorithm that solves the GPe equation has been introduced. We are ready to define the main problem of the thesis.

2.4 Emission of Jets

This section is dedicated to introducing the phenomenon that will be studied and what aspects this thesis will focus on. The first subsection will talk about how the phenomenon occurs and what makes it interesting. The second subsection is dedicated to making the GPe equation model the problem. In the third subsection, the physical parameters of the problem are defined. Finally the different trap shapes that were used will be illustrated and their physical parameters defined.
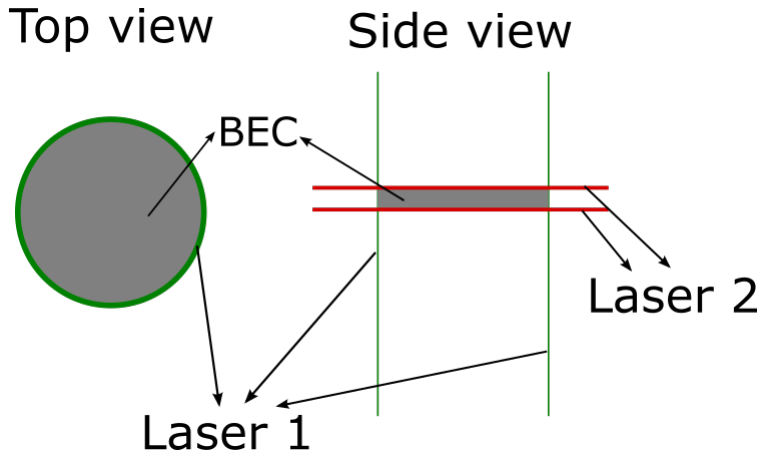
2.4.1 The Problem

Figure 2.1: Experimental setup in a top view and side view. The light grey color indicates the shape of the trapped BEC and two types of lasers labelled laser 1 (green) and laser 2 (red). Laser 1 acts as a finite well potential that shapes the BEC into a cylinder and laser 2 acts as a harmonic potential that squashes the cylinder into a disk making a 2D system.

In 2017, the researchers at Chicago university had discovered a new phenomenon related to the BEC [25]. In their experiment they trapped a BEC using two lasers. One of the lasers was used to shape the BEC into a cylinder while the other was used to squash the BEC into a 2D disk. Figure 2.1 shows the experimental setup. The BEC itself was made up of cesium atoms and by using Feshbach resonance the group were able to change the scattering lengths between the atoms in a sinusoidal pattern. As a consequence, they observed jets escaping the trap along the circumference of the disk. It was noted that these jets formed an asymmetric pattern i.e. the number of particles emitted along one direction was more than the opposite direction.

2.4.2   Modelling the Problem

Since the system is constantly being driven it reasonable to use the time-dependent GPe

$$i\hbar\frac{\partial\Phi}{\partial t} = -\frac{\hbar^2}{2m}\nabla^2\Phi + V_{\text{ext}}(\vec{r})\Phi + Ng|\Phi|^2\Phi.$$

for modelling the problem. We can start by defining the external potential. We use

$$V_{\text{ext}}(\vec{r}) = \left\{ \begin{array}{ll} 0, & \text{for } |\vec{r}| \leq R_{\text{in}} \\ V_0, & \text{for } R_{\text{in}} \leq |\vec{r}| \leq R_{\text{out}} \\ 0, & \text{for } R_{\text{out}} \leq |\vec{r}| \end{array} \right\}$$

where $R_{\text{in}} < R_{\text{out}}$. The external potential has a finite width instead of a single line to prevent any leaks in the simulation. The next effect to take care of is the periodically modulating scattering length. In the GPe the scattering potential g is responsible for controlling the scattering lengths. For our purposes $g(t)$ should depend on time. In the experiment described in the previous section the scattering lengths were modulated according as [25]

$$a(t) = a_{\text{dc}} + a_{\text{ac}}\sin(\omega t) \tag{2.23}$$

where a_{dc} is a small positive constant scattering length, a_{ac} is the modulated scattering length and ω is the modulation frequency. This suggests that the scattering potential have form

$$g(t) = g_{\text{dc}} + g_{\text{ac}}\sin(\omega t). \tag{2.24}$$

Since this is a two dimensional problem 2D scattering potentials are used. Therefore [33]

$$g_{\text{dc}} = \sqrt{8\pi}\frac{\hbar^2}{m}\frac{a_{\text{dc}}}{a_z}. \quad g_{\text{ac}} = \sqrt{8\pi}\frac{\hbar^2}{m}\frac{a_{\text{ac}}}{a_z}, \quad \text{where} \quad a_z = \sqrt{\frac{\hbar}{m\omega_z}}.$$

where ω_z is the angular frequency of the harmonic potential used to squash the BEC. Plugging equation (2.24) into the GPe gives

$$i\hbar\frac{\partial\Phi}{\partial t} = \left[-\frac{\hbar^2}{2m}\nabla^2 + V_{\text{ext}}(\vec{r}) + N(g_{\text{dc}} + g_{\text{ac}}\sin(\omega t))|\Phi|^2 - g_{\text{dc}}n_0 \right]\Phi. \tag{2.25}$$

where we have subtracted by $g_{\text{dc}}n_0$, where n_0 is the average density of the ground state. Since this new term is a constant it can be absorbed into the external potential. If we were to

find the ground state of the system and then study the behaviour of the BEC by modulating its scattering length, we would see circular ripples of matter escaping the trap similar to the ripples formed when a stone is dropped in water. This behaviour was not observed in the experiment. An additional step is needed to resolve this. One way to make the GPe have good phenomenological agreement is by taking the ground state then adding random fluctuations to the wavefunction.This additional step is justified because in an experiment a BEC can never be cooled to 0 K, which means that there will be some thermal noise in the system. Once this step is added, then propagating the ground state through real-time predicts asymmetric jets like observed in the experiment.

In this thesis the random fluctuations used are [26]

$$\psi_f = \epsilon_1 + i\epsilon_2 \tag{2.26}$$

where ϵ_1 and ϵ_2 are real Gaussian distributed random numbers with mean equal 0 and variance equals $0.1|\psi_0|$ where ψ_0 is the ground state. The choice of $0.1|\psi_0|$ gives jets with widths that are similar to the physical case. With the model ready in the next subsection the physical parameters of the system with a circular trap are defined.

2.4.3 Physical Parameters

The physical parameters used in this thesis are directly taken from the experiment conducted in [26]. They are as follows: number of particles $N = 40,000$, the mass of each particle $m = 132.905$ a.m.u, the height of the potential $V_0 = h \times 200$ J, the harmonic potential frequency that squashes the BEC $\omega_z = 220$ Hz, the constant scattering length $a_{dc} = 4a_0$ and the modulating scattering length $a_{ac} = 40a_0$ (where a_0 is the Bhor radius), the modulation frequency $\omega = 620\pi$ Hz and the trap radius $R_{in} = 13$ μm. The outer trap radius for the algorithm is taken as $R_{out} = 1.5R_{in}$.
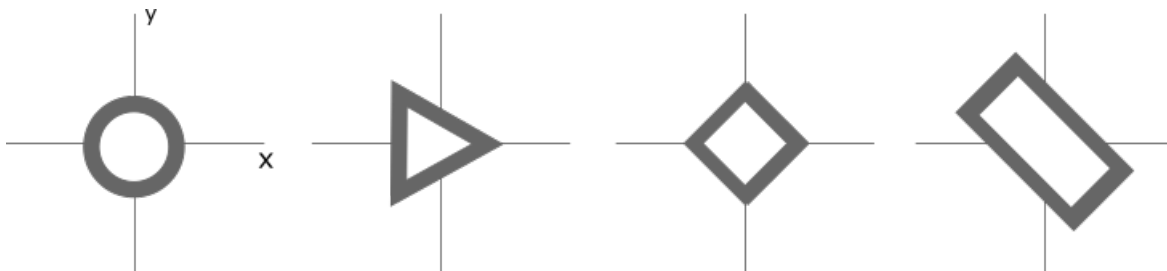
2.4.4 Trap Geometries

Figure 2.2: Four different traps for which the firework patterns are studied in this thesis. The first one is the circular trap, the second position shows an equilateral triangle, the third position shows a square and last position shows a rectangle. The grey boundaries for all the traps have $V = 200 \times \hbar$ J. The white region for all the traps have $V = 0$. The x and y directions are indicated on the axis of the first trap.

In this thesis other than replicating the results of the circular trap from [26], three additional trap geometries are studied. Namely, an equilateral triangle, a square and a rectangle. The shapes of the traps can be seen in figure 2.2. For the all the traps the area within the boundary is set to $A = \pi R_{\text{in}}^2 = \pi \times 13^2\ \mu m^2$. This chosen so that initial density of BEC for all cases are the same.

2.5 Parametric Resonance

For the jets to be emitted the scattering length of the BEC needs to be periodically modulated. Suggesting that the system undergoes parametric resonance. It would be interesting to see the relation between the resonating wavenumbers and physical parameters. To this end, we study the behaviour of the system at small length and time scales. In this regime the wave function can be linearized as [26],

$$\psi = \psi_0[1 + \nu(\vec{r}, t)], \tag{2.27}$$

where $\psi_0 = \sqrt{(n_0)} \exp(iU_1 n_0 \cos(\omega t)/\omega \hbar)$ and $|\nu(\vec{r}, t)| << 1$. $\nu(\vec{v}, t)$ can be viewed as a variation over the uniform BEC therefore it can be written as

$$\nu(\vec{r}, t) = (\xi(t) + i\zeta(t)) \cos(\vec{k} \cdot \vec{r} + \phi), \tag{2.28}$$

where ϕ is a phase term and $\vec{k}$ is the wave number. Inserting equation equation (2.27) into the time dependent GPe equation and ignoring trap effects gives the following set of differential equations,

$$\frac{d^2\xi}{dt^2} + \Omega^2[1 + \alpha \sin(\omega t)]\xi = 0, \tag{2.29}$$

$$\frac{d^2\zeta}{dt^2} - \alpha\omega \cos(\omega t)\frac{d\zeta}{dt} + \Omega^2[1 + \alpha \sin(\omega t)]\zeta = 0, \tag{2.30}$$

where $\Omega^2 = \hbar^2 k^4/(4m^2) + g_{\text{dc}} n_0 k^2/m$, $\alpha = g_{\text{ac}} n_0 k^2 m/\Omega^2$, k is the wavenumber and ω is the modulation frequency. The full derivation can be found in appendix B. Equations (2.29) and (2.30) are known as the Mathieu equations and are used to model systems that have parameters periodically changing [34]. The solutions for equations (2.29) and (2.30) are [26]

$$\xi(t) \approx A_+ \cos(\omega t/2 + \theta_+) \exp(\lambda_+ t) + A_- \sin(\omega t/2 + \theta_-) \exp(\lambda_- t), \tag{2.31}$$
$$\zeta(t) \approx -A_+ \sin(\omega t/2) \exp(\lambda_+ t) + A_- \cos(\omega t/2) \exp(\lambda_- t), \tag{2.32}$$

where,

$$\lambda_\pm = \pm\sqrt{\frac{\alpha^2\Omega^2}{16} - (\Omega - \frac{\omega}{2})^2}. \tag{2.33}$$

The solutions are a linear combination of an exponential growth and exponential decay term. Since we expect the resonating waves to grow we look at when λ_+ is at its maximum. This is only the case when $\Omega - \omega/2 = 0$. Assuming $g_{\text{dc}} \approx 0$ the equation

$$\Omega - \frac{\omega}{2} = \frac{\hbar k^2}{2m} - \frac{\omega}{2} = 0,$$

if

$$k = \sqrt{\frac{\omega m}{\hbar}}. \qquad (2.34)$$

The resonating wavenumber is called k_f henceforth. As we can see the resonating wavenumber solely depends on the mass of the individuals atoms in the BEC and the modulation frequency.

To summarize this section. The system we studied has its scattering length periodically modulated. By looking at small length and time scales we assumed that the BEC would be mostly uniform with some infinitesimal variations. By ignoring trap effects it was possible to derive the Mathieu equations. The solution to these equations allowed us to find what wavenumbers would resonate.

Chapter 3

Results

In this chapter we will present the results and discussion. The structure of this chapter is as follows: Firstly, parameters used for all the results will be defined. After that, the main results for circular case will be given and discussed. Finally, the results and discussion for the polygon traps will be given.

3.1 Parameters

The following parameters were used in all the simulations: The number of particles $N = 40{,}000$, the mass of each particle $m = 132.905$ a.m.u, the height of the potential $V_0 = h \times 200$ J, the harmonic potential frequency that squashes the BEC $\omega_z = 220$ Hz, the constant scattering length $a_{dc} = 4a_0$ and the modulating scattering length $a_{ac} = 40a_0$ (where a_0 is the Bhor radius), the modulation frequency $\omega = 620\pi$ Hz and the trap radius $R_{in} = 13$ μm. The outer trap radius for the algorithm is taken as $R_{out} = 1.5R_{in}$. These parameters are taken from [26]. For the remaining polygonal traps we set the length of the sides such that the area in the trap was $A = \pi R_{in}^2 = \pi$. The BEC and traps were initalized in a 520×520 μm^2 box. Each dimension of the box had 1024 points, giving a total of 1024×1024 points in the whole box.
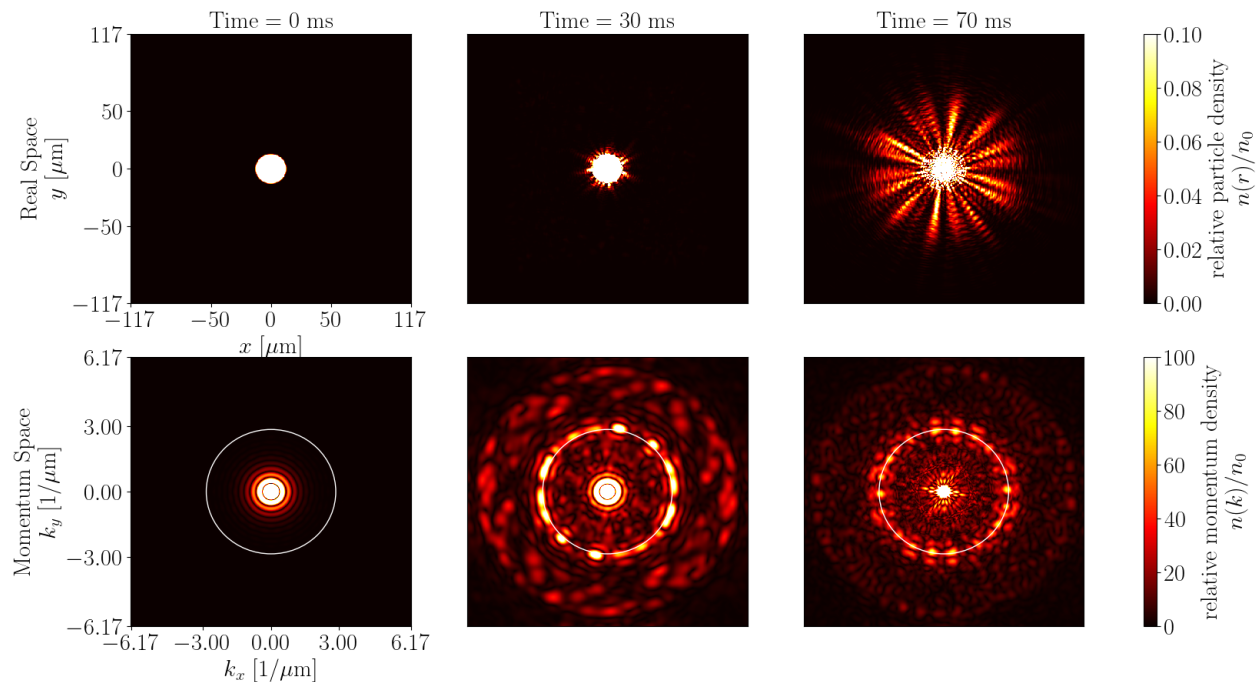
3.2 Circle Trap

Figure 3.1: Shows the evolution of a BEC in a ciruclar trap when its scattering length is periodically changed. In the top row and bottom row its relative density distribution $n(r)/n_0$ and relative momentum density distribution $n(k)/n_0$ can be seen respectively, where n_0 is the average density of the initial BEC. The relative density distribution shows the progression of the jets. In the relative momentum distribution plots, a white circle of radius k_f is drawn, where k_f is the predicted magnitude of resonating wavenumbers. The plots show the appearance of the resonating wavenumbers near the circle.

This section is dedicated to replicating the results from [26]. In order to do this, we will define several observables which will help with understanding how the formation of jets emerges from the BEC.

To replicate the results we used the time-dependent GPe and numerically solved it. An additional step of adding noise to the wavefunction before real-time propagation is needed. Without the noise the jets observed in the top row of figure 3.1 would not occur. Instead, circular ripples of matter moving outwards would be seen. One physical reason for adding the noise would be that in an experiment a BEC is never cooled to 0 K. Therefore there will always be some thermal noise in the system.

Figure 3.1 shows the density plots of a BEC in a circular trap. The top row shows the evolution of the relative density distribution $n(r)/n_0$ (where n_0 is the initial density of the BEC) at times 0, 30 and 70 ms. All the plots in the top row share the same colour bar that has a max value of 0.1, so densities of 0.1 or higher will all appear white. The value of

0.1 allows us to see the jets. We note that the maximum relative density of ground state is approximately 1.7. The bottom row shows the evolution of the relative momentum density at times 0, 30 and 70 ms. In each plot, a white circle is drawn. This circle has a radius of k_f which signifies where the resonating wavenumbers should form. All the plots in the bottom row share the same colour bar that has a max value of 100. The value of 100 allows us to see the resonating wavenumbers.

We start by looking at the top row. At 0 ms, we see the ground state of the system. At 30 ms, a few jets have appeared. The tips of the jets have escaped the trap, but there are still portions under the influence of the trap. This is because the trap has a finite width. At 70 ms, these jets have had time to evolve. At the base of these jets, we can see a highlighted circular region. This region is the finite width of the trap.

In the bottom row, at 0 ms, we see the ground state of the system in momentum space. At 30 ms, the resonating wavenumbers near the white circle have appeared. At 70 ms, the resonating wavenumbers can still be seen near the white circle, but their amplitude is not as high as before.

We derived the resonating wavenumber $k_f = \sqrt{\omega m/\hbar}$ by ignoring trap effects and assuming that the centre of the BEC was uniform at small time and length scales. This means the resonating wavenumbers that appear in the figure should not depend on trap the shape. Note that the jet pattern is dependent on the initial seed of random numbers that is added to the ground state of the BEC, before periodically modulating its scattering length. The density plots in figure 3.1 show one possible jet pattern.

We can study the build-up of these resonating wavemodes by finding the total amplitude in the circular resonating region. We introduce a quantity called the density wave amplitude A_k to do this. It is defined as

$$A_k = \frac{1}{n_0} \int_{-(k_f+5)}^{(k_f+5)} \int_{-\sqrt{(k_f+5)^2-k_x^2}}^{\sqrt{(k_f+5)^2-k_x^2}} |\tilde{n}(\vec{k})| dk_y dk_x - \frac{1}{n_0} \int_{-(k_f-5)}^{k_f-5} \int_{-\sqrt{(k_f-5)^2-k_x^2}}^{\sqrt{(k_f-5)^2-k_x^2}} |\tilde{n}(\vec{k})| dk_y dk_x. \quad (3.1)$$

where n_0 is the initial density of the BEC and $\tilde{n}(\vec{k})$ is the Fourier transform of the BEC density distribution $n(\vec{r})$. The integration boundaries are chosen to solely include the resonating region which appearsbetween circles of radii $k_f \pm 5$.
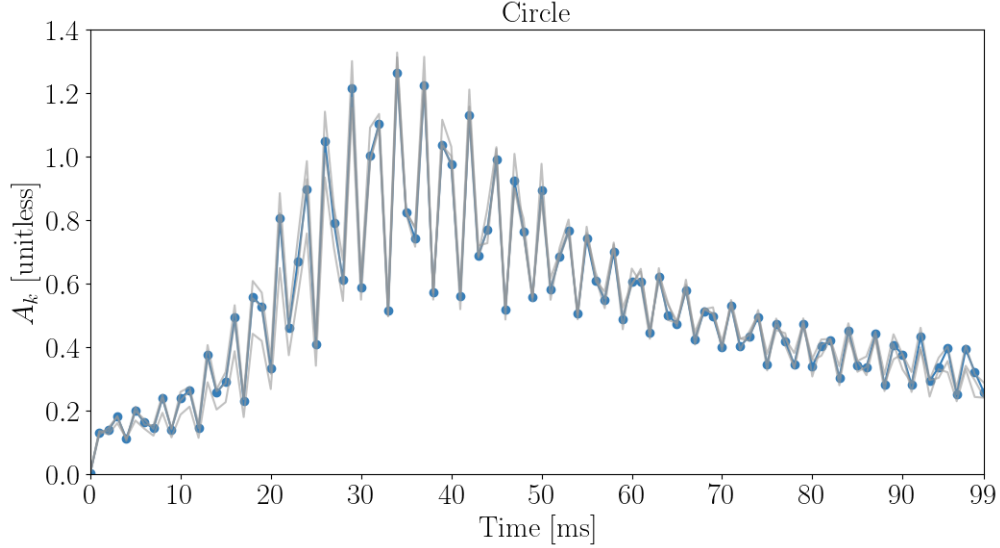
Figure 3.2: The density wave amplitude A_k vs time for the circle. A_k is computed according to eq (3.1). There are four lines in the figure. The three grey lines show how A_k progresses in time for three different initial seeds. The blue dots show the average A_k over five different initial seeds and the blue line just connects the blue dots. The interval between each data point is 1 ms and there are a total of 100 data points.

Figure 3.2 shows the density wave amplitude A_k vs time. The blue dots show the average data points where the average is taken over five different seeds. Furthermore, the three grey lines show A_k for three different initial seeds. There is an oscillatory pattern in the figure. This is a direct consequence of periodically changing the scattering length of the BEC. In addition, the figure can be broken into the following intervals: From 0 to 20 ms, there is a rise in A_k. From 20 to 40 ms, A_k continues to grow until reaching a plateau. Finally, from 40 to 99 ms, there is a decrease in A_k.

The rapid growth in A_k is connected to the amplitude of the resonating waves increasing before the jets are released from the trap. The subsequent drop in A_k is connected to the jets being released. This is evident from the density plots shown in figure 3.1. At 30 ms, jets can be seen. But, a portion of them is still under the influence of the trap. Therefore, at 30 ms the jets have not been fully released from the trap.

Looking back at figure 3.1, the resonating wavenumbers at 30 ms do not have a homogeneous distribution. Furthermore, the emitted jet population at 70 ms is also not homogeneous. To study these distributions, we can define two observables called the structure factor $S(k_f, \phi)$ and emitted jet population $N(\phi)$ where ϕ is the polar angle. These observables can be used to see if there is any correlation between the resonating wavenumbers and emitted jet population distributions. The structure factor is defined as

$$S(k_f, \phi) = \frac{1}{N_0} \int_{k_f-5}^{k_f+5} |\tilde{n}(\vec{k})|^2 k \, dk \qquad (3.2)$$

19

where N_0 is the initial number of particles in the BEC. While the emitted jet population is defined as

$$N(\phi) = \int_{r_0}^{(|\vec{r}|=L_x)} r n(\vec{r}) dr \qquad (3.3)$$

where $n(\vec{r}) = |\Psi(\vec{r})|^2$ is the density distribution, L_x is the length of the square box in which the trap and BEC are initialized, and r_0 is the position vector that points to the outer boundary of the trap.
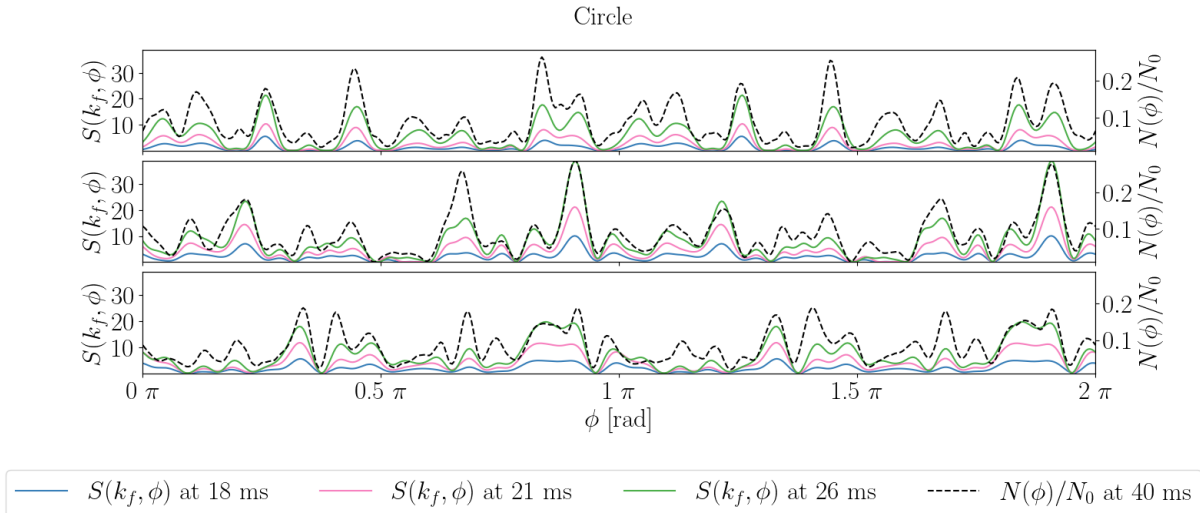

Figure 3.3: The structure factor $S(k_f, \phi)$ vs angle distribution and emitted jet population $N(\phi)/N_0$ (N_0 is the initial number of particles) vs angle from the circle trap. Each row corresponds to a different initial seed. The solid colored lines show the structure factor $S(k_f, \phi)$ of the BEC at different times and the dashed black lines corresponds to the emitted jet population $N(\phi)$. The times for each line is indicated in the legend at the bottom.

When comparing the distributions of the solid lines in the three subplots in figure 3.3, notice how they differ from each other. This suggests, that different initial seeds give different $S(k_f, \phi)$. Looking at the solid lines in each subplot, the amplitude of the peaks grows but the distributions do not change. This implies that once the $S(k_f, \phi)$ is chosen at an early time it does not change. Furthermore, there is a correlation between the structure factor before the emission of jets and the emitted jet population at a later time [26].

To understand what the results from figure 3.3 signify, suppose the scattering length of the BEC is periodically modulated. Then the particles in the BEC start forming resonating waves of matter. Let one of these waves of matter move along direction $\vec{k}$ where $|\vec{k}| \approx k_f$. Then this wave of matter will continue to build up in amplitude because $S(k_f, \phi)$ stays constant and only changes in amplitude. Since there is a correlation between $N(\phi)$ and $S(k_f, \phi)$, we expect that when the wave of matter leaks out of the trap as a jet, its direction is still along $\vec{k}$ [26].

Since we expect a jet to originate from a resonating wave of matter, we may expect that there is always a correlation between $S(k_f, \phi)$ and $N(\phi)$. To test this, we can see how the emitted jet population looks like at an early time and a later time. Figure 3.4 shows the emitted jet population $N(\phi)/N_0$ vs angle ϕ at different times. The figure has three rows which correspond to different initial seeds and two columns which correspond to times 40 and 70 ms.
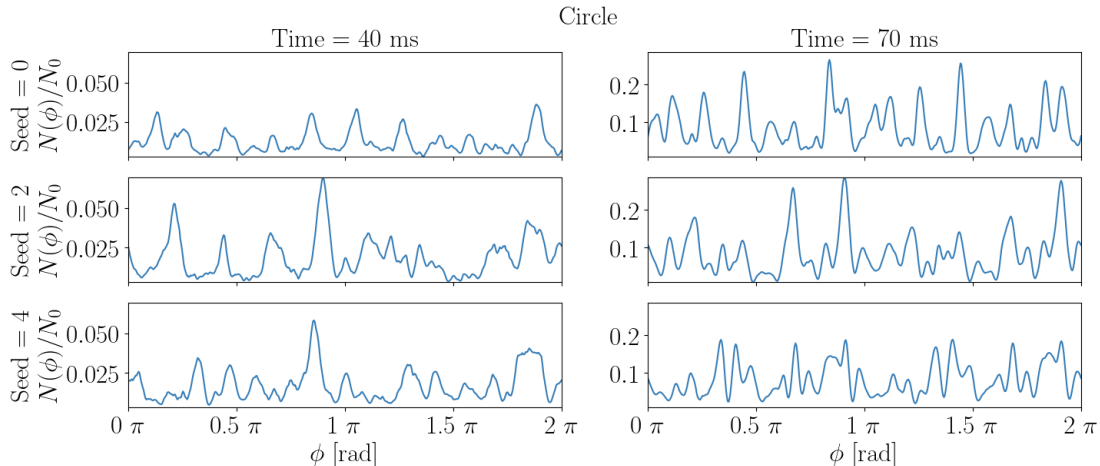

Figure 3.4: The emitted population $N(\phi)/N_0$ vs angle ϕ for the circle trap, where N_0 is the initial number of particles. Each column has a given time labelled on top. Each row has a different seed labelled on the left. The figure shows how $N(\phi)$ at 40 and 70 ms look different from each other.

When looking at each row of the figure 3.4, we see that $N(\phi)$ at 40 ms and $N(\phi)$ at 70 ms are different. This is due to the interference between the different jets that are leaving the trap [26]. From the results, we can conclude that there is no correlation between $S(k_f, \phi)$ and $N(\phi)$ at early times.

To summarize the results from figures 3.3 and 3.4. In figure 3.3 we see that there is a correlation between the $N(\phi)$ and $S(k_f, \phi)$ at 70 ms. But figure 3.4 there is no correlation between $N(\phi)$ at 40 ms and 70 ms. As a result there is no correlation between $N(\phi)$ and $S(k_f, \phi)$ at 40 ms.

Since we have shown that $N(\phi)$ changes as time progresses, we can track how its asymmetry changes with time. We define the asymmetry in coordinate space as [26]

$$\eta_r = \frac{\langle [N(\phi) - N(\phi + \pi)]^2 \rangle}{\langle N(\phi) \rangle^2}, \tag{3.4}$$

where η_r is the average number of particles emitted at angles ϕ and $\phi + \pi$ for $\phi \in [0, \pi]$. Therefore, $\eta_r = 0$ would imply that a jet pattern is perfectly symmetric but need not be uniform. Furthermore, the asymmetry in momentum space can be defined as [26]

$$\eta_k = \frac{\langle [\tilde{N}(\phi) - \tilde{N}(\phi + \pi)]^2 \rangle}{\langle \tilde{N}(\phi) \rangle^2}, \tag{3.5}$$

21

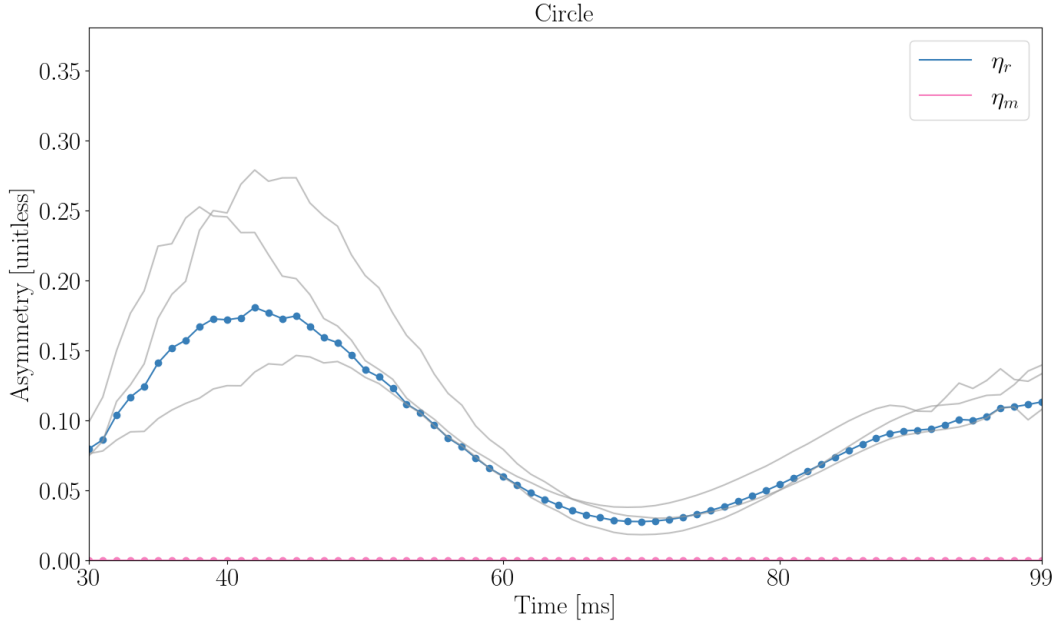where $\tilde{N}(\phi)$ is the Fourier transform of $N(\phi)$.

Figure 3.5: The asymmetry of emitted jets η_r vs time and the asymmetry in momentum space η_k vs time for the circular trap case. The blue and pink dots show the average η_r and η_k, where the average is taken over five different initial seeds. The grey lines show the asymmetry in coordinate space for three different seeds. The figure shows that the total asymmetry in momentum space η_k is 0.0 for all time implying that momentum is conserved. It also shows that the asymmetry of the emitted jets changes η_r with time.

By looking at the asymmetry of the resonating wavenumbers, the conservation of momentum can be checked. Figure 3.5 shows the average asymmetry of the distribution in real space η_r and the distribution in momentum space η_k. The pink line that is flat shows $\eta_k = 0.0$ all time, which means the Fourier transform of the density distribution $n(\vec{r})$ is symmetric. As a consequence momentum is conserved in the system [26].

Since the conservation of momentum holds, for any resonating wave travelling in the $\vec{k}_1$ direction, we should expect another wave travelling in the $-\vec{k}_1$ direction with equal amplitude. But suppose, there is another wave that travels along $\vec{k}_2$. Let the angle between $\vec{k}_1$ and $\vec{k}_2$ be $\delta\theta$ which is small. Such waves exists in the system because $S(k_f, \phi)$ in figure 3.3 has broad peaks. Then as jets are emitted along $\vec{k}_1$ and $\vec{k}_2$ they interfere with each other. Due to momentum conservation, jets would also be emitted along $-\vec{k}_1$ and $-\vec{k}_2$ and interfere with each other. If the jets along $\vec{k}_1$ and $-\vec{k}_1$ are correlated and the same is true for jets along $\vec{k}_2$ and $-\vec{k}_2$, the interference pattern would be the same on both sides. If the previous assumption were true for all jets then we would see a symmetric emitted jet pattern.

The blue line in figure 3.5 shows the η_r. It starts with a non zero value and increases for

a short interval. Then starts decreasing in value until hitting a minimum. After that, the asymmetry increases again.

The fact that η_r starts with a non zero value suggests that jets being emitted on opposing sides are not correlated to one another. The initial increase in asymmetry can be explained by interference between the jets as they just leave the trap. The gradual decrease in asymmetry corresponds to the jets spreading out which reduces the interference between close-by jets. The lack of interference makes the jet pattern more symmetric [26]. The general expectation would be that the asymmetry continues to reduce and stabilise close to zero as the jets spread out. But, the asymmetry starts increasing after hitting the minimum. There is no evidence of a secondary build up and release from A_k. This eliminates the possibility of a secondary release of jets. Assuming that the predictions of the GPe are still accurate in this regime, the only explanation is interference. We note when looking at the density plots in real space, as the jets continue to spread out, new jets that were hidden appear after 70 ms. This suggests that we may not have evolved the system for a long enough time. With the current parameters used to obtain these results, doing a longer real-time evolution would allow the jets to reach the boundaries.

For the remaining results, we will answer whether all the conclusions in this section hold for the polygon traps. In the next section we will only look at the density plots for the different traps.

3.3   Density and Momentum Plots for Polygonal Traps

Since we have expressed the main ideas of analyzing the structure of the jets in the circular trap case, the current and next sections will only look at one result at a time for all the polygonal traps. For example, this section compares the density plots, while the next section looks at the density wave amplitude A_k.

In this section, figures 3.6, 3.7 and 3.8 show the density distributions of the BEC in the equilateral triangle, square and rectangle traps respectively. In each figure, there are two rows and three columns. Each row has a unique colour bar; the max value of the color bars in the top and bottom row are chosen to make the jets and resonating wavenumbers appear clearly. The top row shows the relative density distribution $n(\vec{r})/n_0$ in real space and the bottom row shows the relative momentum distribution $n(\vec{k})/n_0$. A white circle with a radius of the predicted resonating wavenumber k_f is drawn in each plot on the bottom row. Each column from left to right shows the distributions at 0, 30 and 70 ms.

The square and the equilateral triangle traps emit the majority of the jets from their sides. Yet, we can see differences at the vertices between the two traps. The square trap emits more particles along its vertices than the triangle trap. Furthermore, at 70 ms, the emitted jets from the equilateral triangle trap spread out. This is not true for the emitted jets from the square, they move straight.
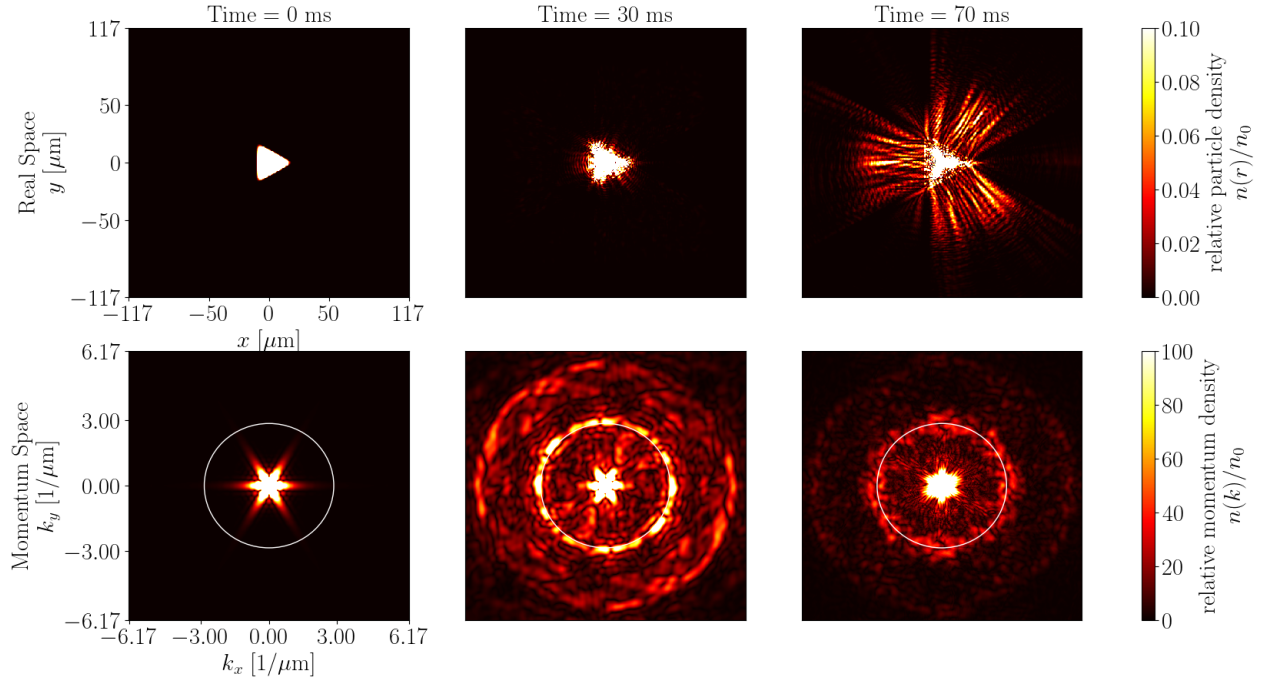
23

Figure 3.6: Same as figure 3.1 but for the equilateral triangle trap.
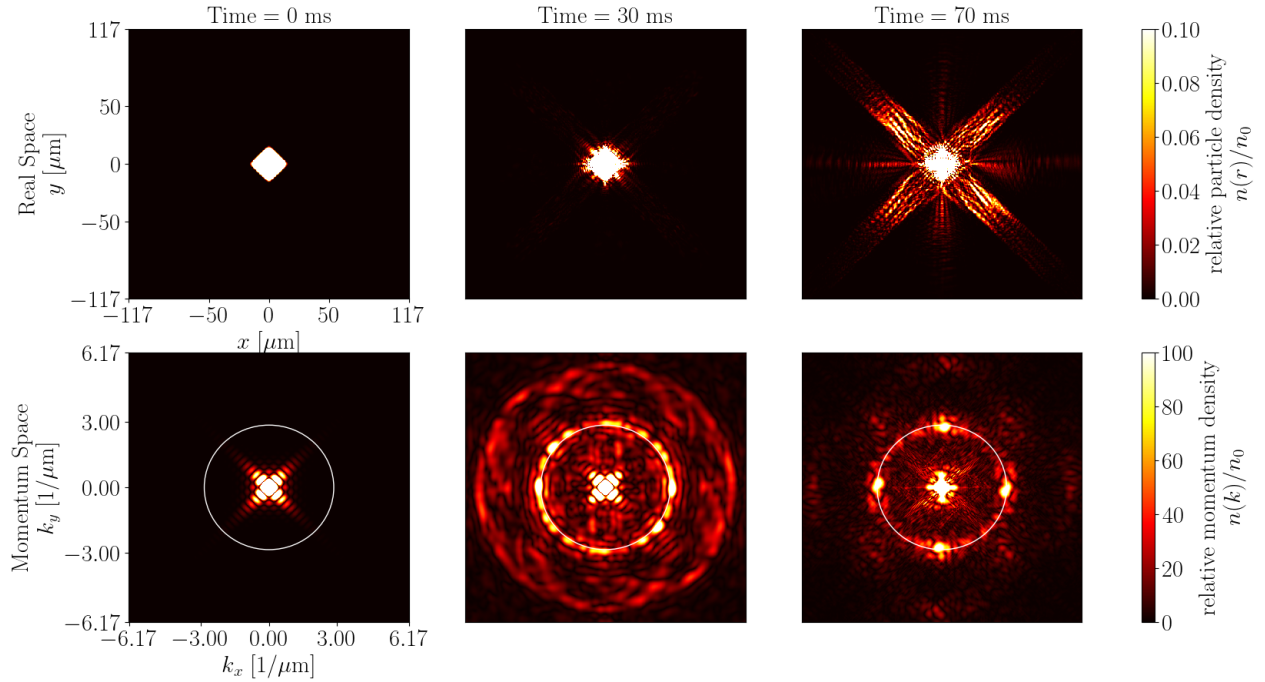

Figure 3.7: Same as figure 3.1 but for the square trap.

A large emission of jets from the sides of the triangle and square could be due to there being more particles at the sides. Furthermore, we noticed more jets come out of vertices of

24

the square than the equilateral triangle, this could be due to the edge of the square being wider than the equilateral triangle. The next observation was that the jets from the equilateral triangle spread out more than in the square case.

In the relative momentum distirbutions $n(\vec{k})/n_0$ for the equilateral triangle and square, the resonating wavenumbers appear at radius k_f. At 70 ms, the occupied wavenumbers have circular distribution for the equilateral triangle. While for the square, the wavenumbers have a square distribution.

The resonating wavenumbers still appear at k_f for both cases. This means that, the assumption for ignoring the trap shape for the derivation of k_f still holds. The circular and square distribution of wavenumbers that we see in the triangle and square case reflect on the observation that jets spread out from the triangle. While jets move straight away from the square.

Finally, three observations can be made for the rectangle case. Firstly, it emits the majority of particles from its widths (shorter side). Secondly, the resonating wavenumbers still appear at k_f, but the wavenumbers at $2k_f$ are also resonating. Finally, the distribution of the wavenumbers is affected by its shape.

We expected to see the resonating wavenumbers at k_f, because it does not depend on the shape of the trap. But now, wavenumbers at $2k_f$ are resonating. Since these wavenumbers were not resonating for the circle, triangle or square traps, it has to do with shape of the rectangle. Furthermore, the rectangle forces resonating wavenumbers to point along its length. It could be that the lengths are close to the centre of the BEC which affects the build up of waves that point towards to lengths. This could be tested by looking at rectangles with different length to width ratios.
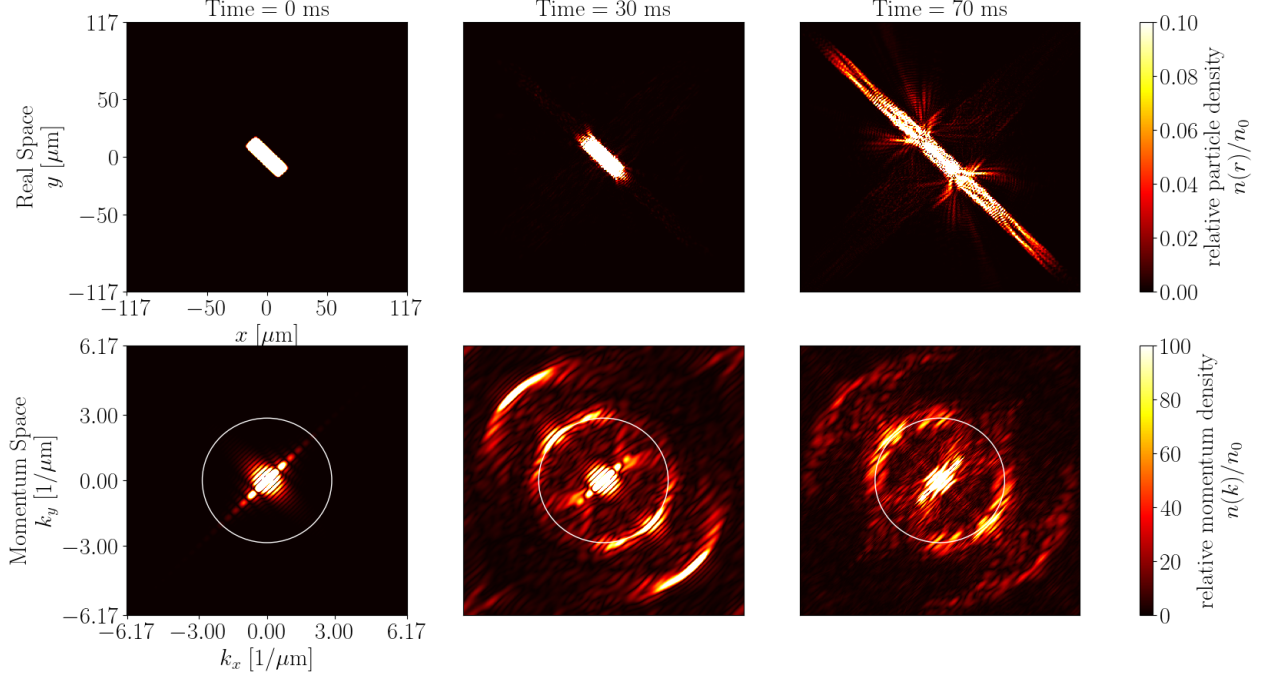
Figure 3.8: Same as figure 3.1 but for the rectangle trap.

3.4 Density Wave Amplitude for Polygonal Traps

Since the resonating wavenumbers still appear at a circle of radius k_f for all polygonal traps, we can study their total amplitude by using A_k (defined in eq 3.1).

Figure 3.9 shows the density wave amplitude A_k vs time for circular, equilateral triangle, square and rectangular traps. Each subplot in the figure can be broken into the following intervals: From 0 to 20 ms A_k increases in value. From 20 to 40 ms A_k continues to increase and then hits a plateau. From 40 to 99 ms A_k reduces in value. With the exception for the square case where the A_k shows an increase in after 80 ms.

In the circular trap case, we connected the sharp increase in A_k to the build-up of resonating wavemodes in the BEC before the emission of jets, and the following reduction of A_k to the jets escaping the traps. These conclusions hold true for all the polygon traps. The shape of A_k before 30 ms for all the subplots in figure 3.9 look similar. From a physical standpoint, A_k depends on the total number of particles that form resonating waves of matter. If there are more particles then A_k is large. The results shows that the process by which these waves grow is not affected by the trap shapes. There is another aspect that all the redsubplots share, it is that the peaks and troughs for A_k align in all cases. For example, if A_k is at a peak at time t for the circle, then A_k is also at a peak at time t for all the polygon traps. The same is true for the troughs. This is because the same modulation pattern is used for all the trap cases.
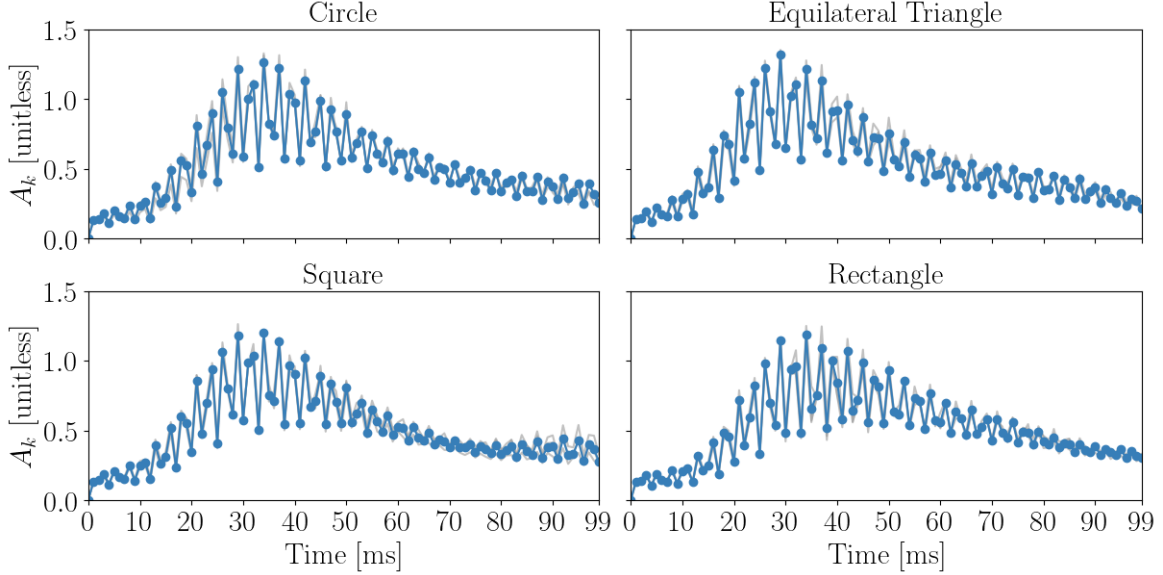
26

Figure 3.9: The density wave amplitude A_k vs time for the circular, equilateral triangle, square and rectangular traps. Each subplot consists of blue dots which is the average A_k computed from five different initial seeds and three grey lines corresponding to A_k for three different initial seeds.

3.5 Structure Factor and Emitted Jet Population for Polygonal Traps

In this section, the structure factor $S(k_f, \phi)$ and emitted jet population $N(\phi)$ for the different polygonal traps are compared. We want to see if there is a correlation between the two like in the circle case.

Figures 3.10, 3.11 and 3.12, show the structure factor $S(k_f, \phi)$ vs angle and emitted jet population $N(\phi)$ vs angle for the equilateral triangle, square and rectangle respectively. In each figure, there are three rows which correspond to different initial seeds. In each row, there exists a blue, pink and green line which corresponds to $S(k_f, \phi)$ at times 18 ms, 21 ms and 26 ms respectively; a dashed black line that corresponds to the emitted jet population at 70 ms and vertical black lines that indicate the position of the polygon vertices.

To understand what figures 3.10 and 3.11 signify, suppose the scattering length of a BEC is periodically modulated. Then, the particles in the BEC start forming resonating waves of matter. Let one of these waves of matter move along direction $\vec{k}$ where $|\vec{k}| \approx k_f$. Then this wave of matter will continue to build up in amplitude because $S(k_f, \phi)$ stays constant and only changes in amplitude. As the wave of matter escapes the trap as a jet, we can no longer expect the jet and the wave of matter to point in the same direction. Because there is no correlation between $S(k_f, \phi)$ and $N(\phi)$. The shape of the trap has affected the direction of the emitted jet.
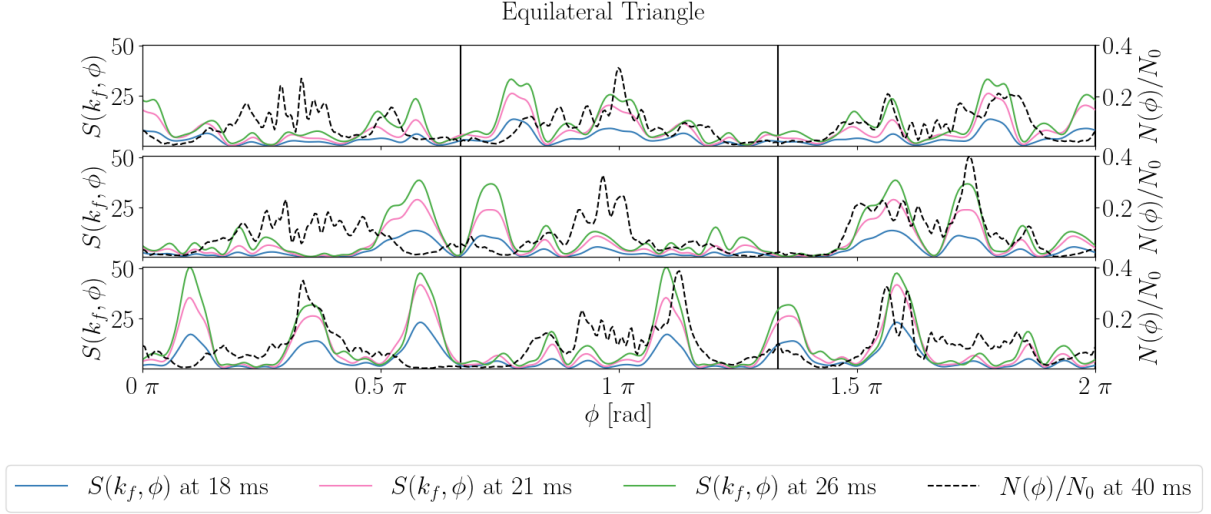
Equilateral Triangle

Figure 3.10: Same as figure 3.3 but for the equilateral triangle trap. The black vertical lines indicates the position of the vertices of the equilateral triangle trap

For different seeds in the rectangle trap, $S(k_f, \phi)$ only has peaks between the black vertical lines. This means that, in all three cases, the widths of the rectangle emit the jets. We see that there is no correlation between $S(k_f, \phi)$ and $N(\phi)$

When comparing these results to the circular trap case we see that the correlation between the $N(\phi)$ and $S(k_f, \phi)$ has been lost for the polygonal traps.
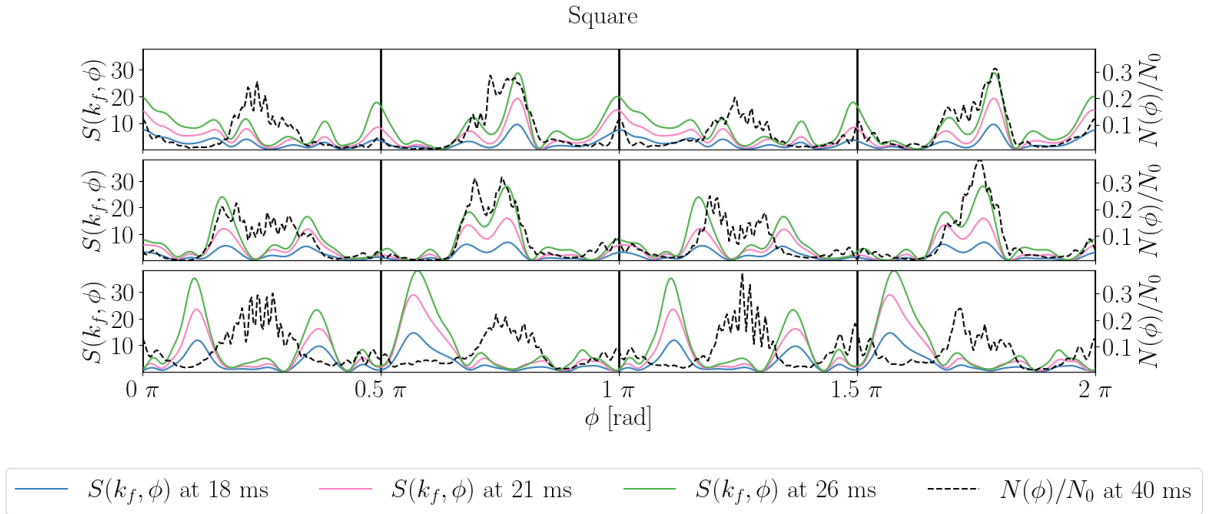
Square

Figure 3.11: Same as figure 3.3 but for the equilateral triangle trap. The black vertical lines indicates the position of the vertices of the square trap
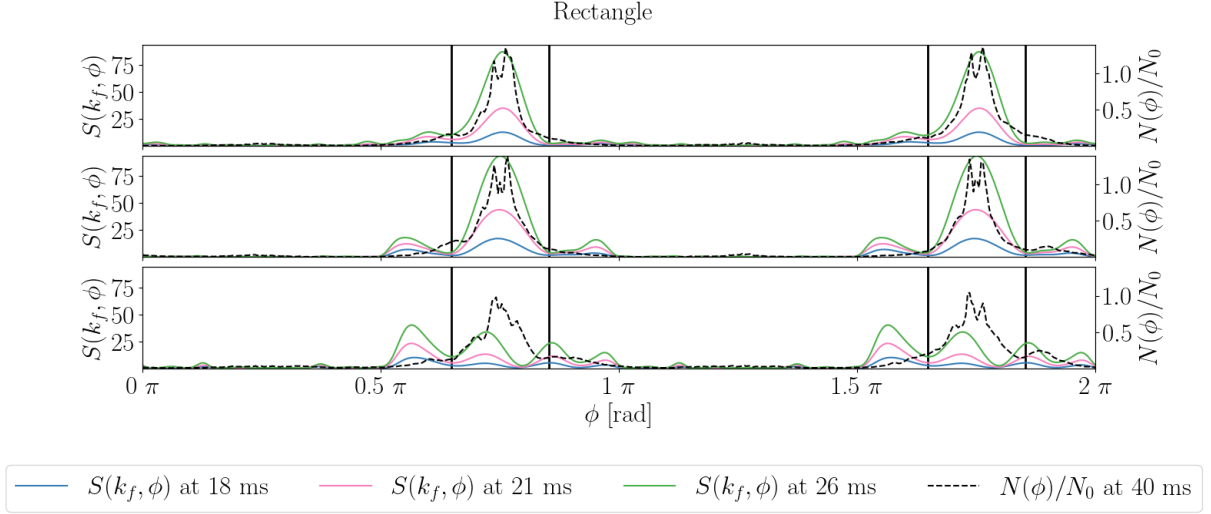
Figure 3.12: Same as figure 3.3 but for the equilateral triangle trap. The black vertical lines indicates the position of the vertices of the rectangle trap

3.6 Emitted Jet Population at Different Times for Polygonal Traps

In this section we will study the $N(\phi)$ for the three polygonal traps at 40 and 70 ms, to see whether there is a change between the jet patterns.
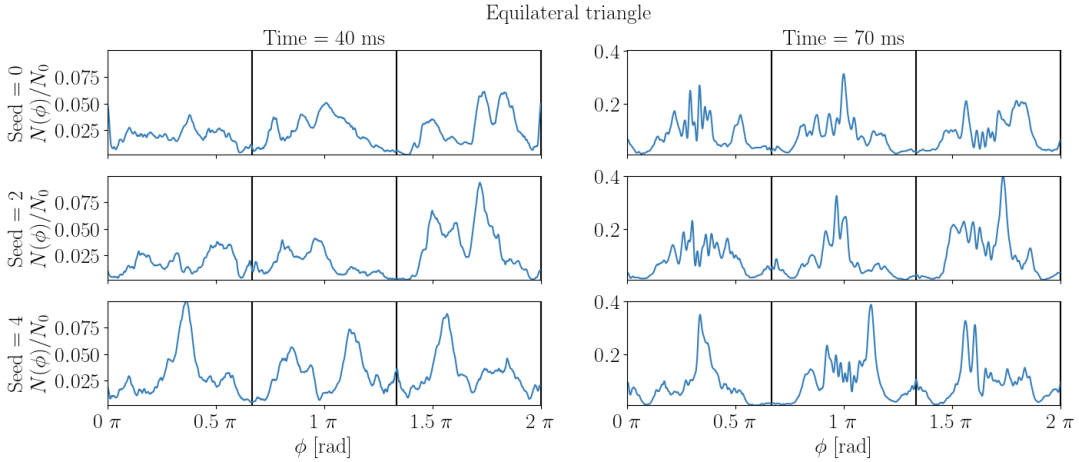

Figure 3.13: Same as figure 3.4. The vertical black lines indicate the position of the vertices of the equilateral triangle trap.

Figures 3.13, 3.14 and 3.15, show the emitted jet population $N(\phi)$ vs angle at different times for the equilateral triangle, square and rectangle traps respectively. In each figure there are three rows which correspond to different initial seeds, two columns which correspond to times 40 and 70 ms; and vertical black lines which indicate the position of the polygon vertices.

The time 40 ms is chosen because the jets right after emission would have time to spread out.

In all the figures, $N(\phi)$ at times 40 and 70 ms look different, for a given seed. This is also the case for the circle. The explanation for the circle is that jets were interfering with each other. This reason should also hold true for the polygon traps, since each side of a polygon emits multiple jets in close proximity.

We now turn to a comparison between the equilateral triangle and square case. For all the seeds, the sides of the traps emit the majority of the particles. This could be because there are more particles near the sides. Furthermore, the square always emitted more particles from its vertices than the triangle. This could be due to the square vertices being wider than the triangle vertices. As a result, the particles have an easier time escaping from the square vertices.

For the rectangle trap, all particles are emitted from its widths. This is in line with the observation that the rectangle forces waves to travel along its length.

Finally, the distribution for the polygons has narrow peaks which make serrated patterns. This is because the sides of the polygon emit the jet in a straight line.
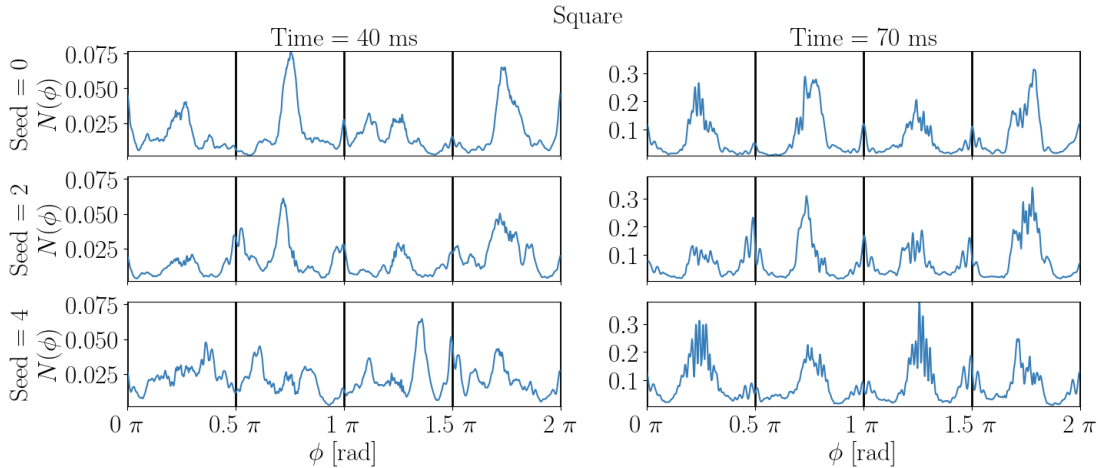

Figure 3.14: Same as figure 3.4. The vertical black lines indicate the position of the vertices of the square trap.
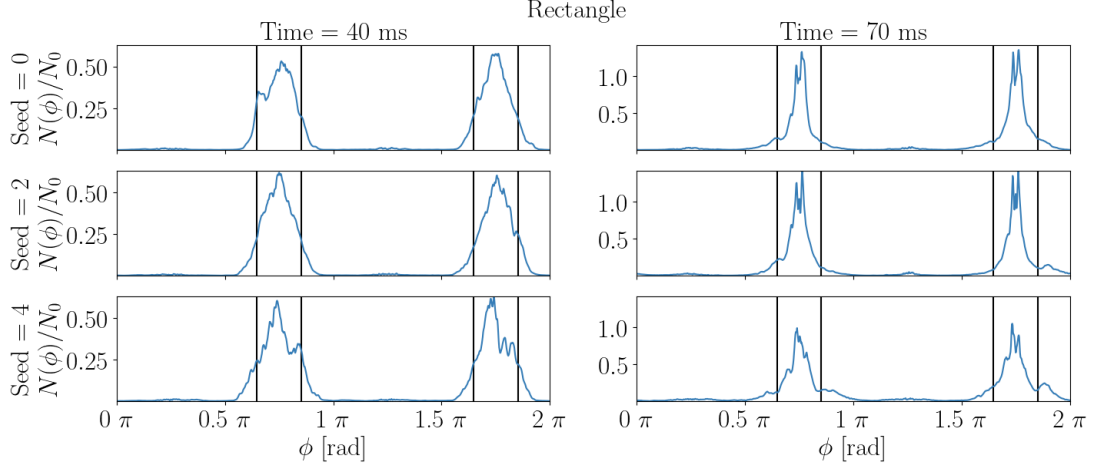
Figure 3.15: Same as figure 3.4. The vertical black lines indicate the position of the vertices of the rectangle trap.

3.7 Asymmetry in Real and Momentum Space for Polygonal Traps

Figure 3.16: The asymmetry of emitted jets η_r vs time and the asymmetry in momentum space η_k vs time for the circular, equilateral, square and rectangular traps. Each subplot consists of blue dots, pink dots and grey lines. The blue dots show the average η_r, the pink dots show the average η_k and the grey lines show η_r for different initial seeds.

In this section, we will see whether the conservation of momentum holds and study the asymmetry of the jets for the polygonal traps.
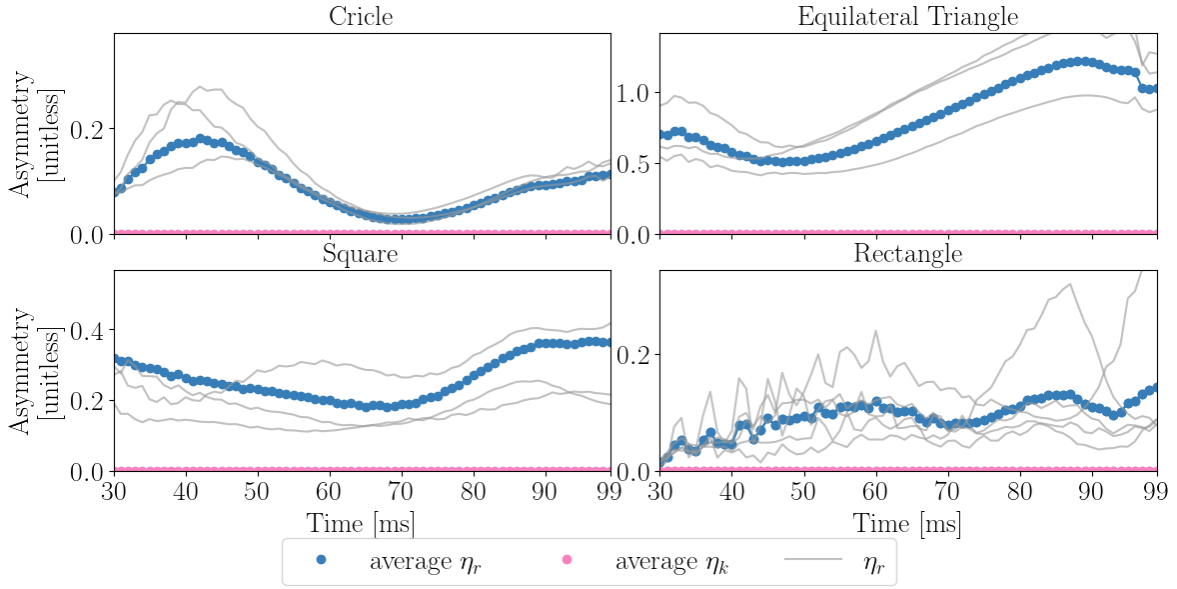
Figure 3.16 shows the asymmetry of emitted jets η_r vs time and asymmetry of momentum η_k vs time for the equilateral triangle, square and rectangle respectively.In all the subplots other than the subplot for the rectangular trap, three grey lines representing n_r have been plotted. In the rectangular case, five grey lines have been plotted to show the large variation in n_r between different initial seeds.

We start by looking at whether the conservation of momentum holds for all the polygon traps. Looking at the figures we see that $\eta_k = 0.0$ for all cases. This confirms that the conservation of momentum holds for all cases. Since the asymmetry in real space for each polygon shows a unique pattern we study them case by case.

Looking at the equilateral triangle case, we see that it starts out with nonzero η_r and then reduces. After hitting a minimum, the η_r starts to rise until hitting a maximum. The initial decrease in η_r is not expected as the equilateral triangle is inherently an asymmetric shape; because all its sides are always opposite to a vertex. We know that majority of the jets escape from the sides of a triangle and little to no jets escape from the vertex. This gives the expectation that the η_r for the equilateral triangle should only rise. However, figure 3.16 shows otherwise. The expected rise only occurs after reaching the minimum. To explain this initial decrease in asymmetry, we look back to figure 3.6 which shows the density plot of the equilateral triangle. Looking at the density plot for 70 ms we see regions along the vertices that do not have jets. However, this effect cannot be seen in the 30 ms plot, because the jets have not had time to spread. Therefore, at earlier times, the lack of jets emitted from the vertices does not contribute significantly to the η_r. The rise in asymmetry should start when the jets have spread out.

Focusing on the square case, η_r reduces until hitting a minimum. After that, it starts starts to rise. We saw in figure 3.7, that the square emits jets in straight lines. Therefore, there is constant interference between the different jets that are emitted from the same side. This means the process by which the asymmetry is reduced for the square case is not the same as in the circle case.

Looking at the rectangular case, it starts out with the lowest η_r out of all the cases. There is no clear pattern to the average η_r as it changes between having a positive gradient and a negative gradient multiple times. Furthermore, all five seeds that were used to calculate the average are plotted in the figure. We see that there can be large variations between different seeds. However, all the seeds consistently start with low asymmetries. To understand why this is the case look back to figure 3.8. There is a large region where no jets exist, which contributes nothing to the η_r. The only region that contribute to the asymmetry is near the widths which are small.

Chapter 4

Conclusions

In conclusion, we numerically simulate the jets released by a BEC trapped in different potentials. In all cases the entire system is not depleted of particles. Instead the BEC is placed in a box big enough to ensure that the emitted jets do not reach the edges of the box and invoke periodic boundary conditions.

When the BEC is in a circular trap, the emitted jets correlate to the directions of the resonating waves before emission. But the correlation is only there when the jets have had enough time to spread out. This is because of strong interference between the jets when they just leave the trap. Furthermore, η_k in momentum space is always equal to zero. This means that conservation of momentum holds. Next, η_r increases, hits a maximum and then gradually decreases until reaching a minimum and increasing again. The initial increase is linked to interference between the jets. The gradual decrease is explained by the jets spreading out and interfering less with each other. The following increase can only be explained by interference.

For the BECs in an equilateral triangle and square trap, they emit the majority of jets from their sides. This is due to more particles being near the sides. Furthermore, the square consistently emitted more jets along its vertices than the triangle. We believe this is due to the vertices of the square being wider than the vertices of the equilateral triangle. The BEC in a rectangle trap only emitted jets from its widths (shorter sides).

For all three polygonal traps, the resonating wavenumbers are found at a circle of radius k_f. We expected this due to the way we derived k_f. But for the rectangle trap forces the resonating wavenumbers to point along its length. Furthermore, the wavenumbers at a circle of radius $2k_f$ are also resonating. We believe this is due to the length of the rectangle being close to the centre of the BEC.

We see that there is a correlation between the emitted jets and the resonating waves for the circular trap case. However, in the polygonal trap cases, the correlation is lost. This is attributed to the trap shapes.

In all the cases conservation of momentum holds. Since the asymmetry of the jets are

unique for each polygon trap, we study them case by case. For the equilateral triangle, the expectation is a continual increase in asymmetry because all its sides are opposite a vertex. But there is an initial decrease in η_r. We attribute this to the jets not having enough time to spread out.

For the square case there was a gradual decrease in η_r. We believe that this gradual decrease is not due to jets interfering less with each other, because the square emits jets in a straight line from its sides. We cannot explain this decrease in asymmetry.

For the rectangle case, it starts out with a low η_r. But there is no consistent pattern for the η_r between different seeds. The only agreement is at 30 ms, where the asymmetry starts close to zero. This is because only the widths emit the jets, which makes a large region have no jets.

Chapter 5

Outlook

This sub-field of ultracold gases is rather new and can be traced back to the experiment done in 2017 [25], where after periodically modulating the scattering length of a BEC, it emitted jets. About a year later, the GPe was found to give good phenomenological agreement between the theoretical predictions and experiments [26]. In 2020, experimental and theoretical work was done on how these jet pattern were affected when the BEC was placed in a circular trap and rotated [35].

There are many avenues that can be explored from this thesis. We noted during our results that the BEC in a square trap emitted more jets from its vertices than one in an equilateral triangle trap. We gave the reason that the vertex of a square is larger than an equilateral triangle. This could be tested by trapping a BEC in a polygon with more than four sides. The expectation is that more jets would be emitted from the vertices. Furthermore, taking inspiration from [35], these polygons could be rotated and the scattering length changed. Looking at the results from [35], there would be a definite effect on the emitted jet pattern. After that, jets being emitted from an ellipse could be studied. The expectation is that, as the ratio between the major and minor axis increases, the resonating wavenumbers would be forced to point along the major axis.

Bibliography

[1] S. N. Bose. Plancks Gesetz und Lichtquantenhypothese, 1924.

[2] A Einstein. Sitzungsber. k. preuss. akad. wiss. 12, 261 (1924).

[3] A Einstein. Sitzungsber. k. preuss. akad. wiss. 1, 3 (1925).

[4] C. J. Pethick and H. Smith. *Bose–Einstein Condensation in Dilute Gases*. Cambridge University Press, 2nd edition, 2008.

[5] E. P. Gross. Structure of a quantized vortex in boson systems. *Il Nuovo Cimento (1955-1965)*, 20(3):454–477, 1961.

[6] L. P. Pitaevskii. Vortex lines in an imperfect Bose gas. *Sov. Phys. JETP*, 13(2):451–454, 1961.

[7] M. H. Anderson, J. R. Ensher, M. R. Matthews, C. E. Wieman, and E. A. Cornell. Observation of Bose-Einstein condensation in a dilute atomic vapor. *science*, 269(5221):198–201, 1995.

[8] C. C. Bradley, C. Sackett, and R. Hulet. Bose-Einstein condensation of lithium: observation of limited condensate number. *Phys. Rev. Lett.*, 78(6):985, 1997.

[9] W. Ketterle. Nobel lecture: when atoms behave as waves: Bose-Einstein condensation and the atom laser. *Rev. Mod. Phys.*, 74:1131–1151, 4, 2002.

[10] E. A. Cornell and C. E. Wieman. Nobel lecture: Bose-Einstein condensation in a dilute gas, the first 70 years and some recent experiments. *Rev. Mod. Phys.*, 74(3):875, 2002.

[11] J. Ensher, D. S. Jin, M. Matthews, C. Wieman, and E. A. Cornell. Bose-Einstein condensation in a dilute gas: measurement of energy and ground-state occupation. *Phys. Rev. Lett.*, 77(25):4984, 1996.

[12] W Fiszdon. Quantized vortices in Helium II. by RJ Donnelly. Cambridge University Press, 1991. 346 pp.£ 95. *J. Fluid Mech.*, 233:691–692, 1991.

[13] D. Butts and D. Rokhsar. Predicted signatures of rotating Bose-Einstein condensates. *Nature*, 397(6717):327–329, 1999.

[14] M. R. Matthews, B. P. Anderson, P. Haljan, D. Hall, C. Wieman, and E. A. Cornell. Vortices in a Bose-Einstein condensate. *Phys. Rev. Lett.*, 83(13):2498, 1999.

[15] J. Williams and M. Holland. Preparing topological states of a Bose–Einstein condensate. *Nature*, 401(6753):568–572, 1999.

[16] A. Leanhardt, Y.-i. Shin, D. Kielpinski, D. Pritchard, and W Ketterle. Coreless vortex formation in a spinor Bose-Einstein condensate. *Phys. Rev. Lett.*, 90(14):140403, 2003.

[17] V. Schweikhard, I Coddington, P. Engels, S. Tung, and E. A. Cornell. Vortex-lattice dynamics in rotating spinor Bose-Einstein condensates. *Phys. Rev. Lett.*, 93(21):210403, 2004.

[18] A. J. Leggett. Bose-Einstein condensation in the alkali gases: some fundamental concepts. *Rev. Mod. Phys.*, 73:307–356, 2, 2001.

[19] S Inouye, A. Chikkatur, D. Stamper-Kurn, J Stenger, D. Pritchard, and W Ketterle. Superradiant Rayleigh scattering from a Bose-Einstein condensate. *Science*, 285(5427):571–574, 1999.

[20] D. Petrov. Quantum mechanical stabilization of a collapsing Bose-Bose mixture. *Phys. Rev. Lett.*, 115(15):155302, 2015.

[21] H. Kadau, M. Schmitt, M. Wenzel, C. Wink, T. Maier, I. Ferrier-Barbut, and T. Pfau. Observing the Rosensweig instability of a quantum ferrofluid. *Nature*, 530(7589):194–197, 2016.

[22] C. Cabrera, L Tanzi, J Sanz, B Naylor, P Thomas, P Cheiney, and L Tarruell. Quantum liquid droplets in a mixture of Bose-Einstein condensates. *Science*, 359(6373):301–304, 2018.

[23] I. Ferrier-Barbut, H. Kadau, M. Schmitt, M. Wenzel, and T. Pfau. Observation of quantum droplets in a strongly dipolar bose gas. *Phy. Rev. Lett.*, 116(21):215301, 2016.

[24] P. Stürmer. Real-time stability and dynamics of vortices in quasi-two-dimensional self-bound two-component Bose-Einstein condensate. eng, 2019. Student Paper.

[25] L. W. Clark, A. Gaj, L. Feng, and C. Chin. Collective emission of matter-wave jets from driven Bose–Einstein condensates. *Nature*, 551(7680):356–359, 2017.

[26] H. Fu, L. Feng, B. M. Anderson, L. W. Clark, J. Hu, J. W. Andrade, C. Chin, and K Levin. Density waves and jet emission asymmetry in Bose fireworks. *Phys. Rev. Lett.*, 121(24):243001, 2018.

[27] L. D. Landau and E. M. Lifshitz. *Quantum mechanics: Non-relativistic theory*, volume 3. Elsevier, 2013.

[28] J Rogel-Salazar. The Gross–Pitaevskii equation and Bose–Einstein condensates. *Eur. J. Phys.*, 34(2):247–257, 2013. ISSN: 1361-6404.

[29] D. F. Schroeter and D. J. Griffiths. Introduction to Quantum Mechanics third edition, 2021.

[30] M. E. Peskin and D. V. Schroeder. *An Introduction to Quantum Field Theory*. Westview Press, 1995. Reading, USA: Addison-Wesley (1995) 842 p.

[31] S. A. Chin and E. Krotscheck. Fourth-order algorithms for solving the imaginary-time Gross-Pitaevskii equation in a rotating anisotropic trap. *Phys. Rev. E*, 72:036705, 3, 2005.

[32] M. N. Tengstrand, P. Stürmer, E. O. Karabulut, and S. M. Reimann. Rotating binary Bose-Einstein condensates and vortex clusters in quantum droplets. *Phys. Rev. Lett.*, 123:160405, 16, 2019.

[33] A. Griffin, D. W. Snoke, and S. Stringari. *Bose-Einstein condensation*. Cambridge University Press, 1996.

[34] L. Ruby. Applications of the mathieu equation. *American Journal of Physics*, 64(1):39–44, 1996.

[35] H. Fu, Z. Zhang, K.-X. Yao, L. Feng, J. Yoo, L. W. Clark, K. Levin, and C. Chin. Jet substructure in fireworks emission from nonuniform and rotating Bose-Einstein condensates. *Phys. Rev. Lett.*, 125:183003, 18, 2020.

Appendix A

Functional Derivatives

A functional derivative of a functional $F(f_1)$, where f_1 is a function, is defined to be

$$\lim_{\epsilon \to 0} \frac{F[f_1 + \epsilon \eta] - F[f_1]}{\epsilon} = \left[\frac{d}{d\epsilon} F[f_1 + \epsilon \eta] \right]_{\epsilon=0}$$

where η is an arbitrary function and ϵ is a parameter. Using the definition above, the functional derivatives of equation (2.5) can be taken.

The term

$$J_{\text{KE}}(\psi, \psi^*) \approx \sum_{i=1}^{N} \frac{\hbar^2}{2m} \int \nabla \psi^*(\vec{r}_i) \nabla \psi(\vec{r}_i) d\vec{r}_i = N \frac{\hbar^2}{2m} \int \nabla \psi^*(\vec{r}) \nabla \psi(\vec{r}) d\vec{r}.$$

This is true because all the wavefunctions for the individual particles are the same. Furthermore, the integration range is all of space. Using Green's identity the $J_{\text{KE}}(\psi, \psi^*)$ can be rewritten as

$$J_{\text{KE}}(\psi, \psi^*) = -N \frac{\hbar^2}{2m} \int \psi^*(\vec{r}) \nabla^2 \psi(\vec{r}) d\vec{r}.$$

The functions ψ and ψ^* in the arguments of J_{KE} can be treated as independent variables [4]. Then taking the functional derivative of $J_{\text{KE}}(\psi, \psi^*)$ w.r.t ψ^* gives

$$\frac{d}{d\epsilon} \left[J_{\text{KE}}(\psi, \psi^* + \epsilon \eta) \right]_{\epsilon=0} = \frac{d}{d\epsilon} \left[-N \frac{\hbar^2}{2m} \int (\psi^*(\vec{r}) + \epsilon \eta(\vec{r})) \nabla^2 \psi(\vec{r}) d\vec{r} \right]_{\epsilon=0}$$

$$= -N \frac{\hbar^2}{2m} \int \eta(\vec{r}) \nabla^2 \psi(\vec{r}) d\vec{r}.$$

The next term is the external potential term. After using the Hartree approximation it becomes

$$J_{\text{Ext}}(\psi, \psi^*) \approx \sum_{i=1}^{N} \int \psi^*(\vec{r}_i) V_{ext} \psi(\vec{r}_i) d\vec{r}_i = N \int \psi^*(\vec{r}) V_{ext} \psi(\vec{r}) d\vec{r}.$$

Taking the functional derivative of $J_{\text{Ext}}(\psi, \psi^*)$ w.r.t ψ^* gives

$$\frac{d}{d\epsilon}\left[J_{\text{Ext}}(\psi, \psi^* + \epsilon\eta)\right]_{\epsilon=0} = \frac{d}{d\epsilon}\left[N\int(\psi^*(\vec{r}) + \epsilon\eta(\vec{r}))V_{ext}\psi(\vec{r})d\vec{r}\right]_{\epsilon=0}$$

$$= N\int\eta(\vec{r})V_{ext}\psi(\vec{r})d\vec{r}.$$

After that, the $J_{\text{PE}}(\psi, \psi^*)$ can be written as

$$J_{\text{PE}}(\psi, \psi^*) \approx \frac{1}{2}\sum_{i=1}^{N}\sum_{j\neq i}^{N}\int d\vec{r_i}\int d\vec{r_j}\psi^*(\vec{r_i})\psi^*(\vec{r_j})V(|\vec{r_i} - \vec{r_j}|)\psi(\vec{r_i})\psi(\vec{r_j})$$

$$= \frac{N(N-1)}{2}\int d\vec{r}\int d\vec{r'}\,\psi^*(\vec{r})\psi^*(\vec{r'})V(|\vec{r} - \vec{r'}|)\psi(\vec{r})\psi(\vec{r'}).$$

Taking the functional derivative gives (denote $\frac{d}{d\epsilon}\left[J_{\text{PE}}(\psi, \psi^* + \epsilon\eta)\right]_{\epsilon=0} = \frac{d}{d\epsilon}J_{\text{PE}}$)

$$\frac{d}{d\epsilon}J_{\text{PE}} = \frac{N(N-1)}{2}\frac{d}{d\epsilon}\left[\int d\vec{r}\int d\vec{r'}\,(\psi^*(\vec{r}) + \epsilon\eta(\vec{r}))(\psi^*(\vec{r'}) + \epsilon\eta(\vec{r'}))V(|\vec{r} - \vec{r'}|)\psi(\vec{r})\psi(\vec{r'})\right]_{\epsilon=0}$$

$$= \frac{N(N-1)}{2}\int\left(\eta(\vec{r})|\psi(\vec{r'})|^2V(|\vec{r} - \vec{r'}|)\psi(\vec{r}) + |\psi(\vec{r})|^2\eta(\vec{r'})V(|\vec{r} - \vec{r'}|)\psi(\vec{r'})\right)d\vec{r}d\vec{r'}$$

$$= N(N-1)\int\left(|\psi(\vec{r'})|^2V(|\vec{r} - \vec{r'}|)\psi(\vec{r})\eta(\vec{r})\right)d\vec{r}d\vec{r'},$$

where the last equality is obtained by renaming the integration variables. Finally, after using the Hartree approximation the $J_{\text{Norm}}(\psi, \psi^*)$ can be written as

$$J_{\text{Norm}}(\psi, \psi^*) \approx -\mu\prod_{i=1}^{N}\left(\int\psi^*(\vec{r_i})\psi(\vec{r_i})d\vec{r_i}\right)$$

$$= -\mu\left(\int\psi^*(\vec{r})\psi(\vec{r})d\vec{r}\right)^N.$$

Taking the functional derivative of $J_{\text{Norm}}(\psi, \psi^*)$ w.r.t ψ^* gives

$$\frac{d}{d\epsilon}\left[J_{\text{Norm}}(\psi, \psi^* + \epsilon\eta)\right]_{\epsilon=0} = \frac{d}{d\epsilon}\left[\left(\int[\psi^*(\vec{r}) + \epsilon\eta(\vec{r})]\psi(\vec{r})d\vec{r}\right)^N\right]_{\epsilon=0}$$

$$= N\int\eta(\vec{r})\psi(\vec{r})d\vec{r}\left(\int\psi^*(\vec{r})\psi(\vec{r})d\vec{r}\right)^{N-1}$$

$$= N\int\eta(\vec{r})\psi(\vec{r})d\vec{r},$$

where the last equality comes from $\int\psi^*(\vec{r})\psi(\vec{r})d\vec{r} = 1$. To minimise the Functional F we set $\frac{d}{d\epsilon}F(\psi, \psi^* + \epsilon\eta)|_{\epsilon=0} = 0$. As a result, the final expression is

$$0 = N\int\left(-\frac{\hbar^2}{2m}\nabla^2\psi(\vec{r}) + V_{ext}(\vec{r})\psi(\vec{r}) + (N-1)\int|\psi(\vec{r'})|^2V(|\vec{r} - \vec{r'}|)d\vec{r'}\psi(\vec{r}) - \mu\psi(\vec{r})\right)\eta(\vec{r})d\vec{r}.$$

Since η is an arbitrary function the expression in the brackets must equal zero giving equation (2.6)

$$-\frac{\hbar^2}{2m}\nabla^2\psi(\vec{r}) + V_{ext}(\vec{r})\psi(\vec{r}) + (N-1)\int |\psi(\vec{r}')|^2 V(|\vec{r}-\vec{r}'|)d\vec{r}'\,\psi(\vec{r}) = \mu\psi(\vec{r}).$$

Appendix B

Parametric Resonance

The following GPe equation is used

$$i\hbar\frac{\partial\psi}{\partial t} = \left[-\frac{\hbar^2}{2m}\nabla^2 + V(\vec{r}) + (U_0 + U_1\sin(\omega t))|\psi|^2 - U_0 n_0\right]\psi. \tag{B.1}$$

If the BEC is viewed at small time scales then the wave function can be linearized as

$$\psi = \psi_0(t)(1 + \nu(t, \vec{r}))$$

where $\psi_0 = \sqrt{n_0}\exp(iU_1 n_0\cos(\omega t)/\hbar\omega)$ is the wavefunction of a uniform BEC and $\nu = (\xi(t)+i\zeta(t))\cos(\vec{k}\cdot\vec{r}+\phi_0)$. The uniform density assumption is true in the center of the trapped BEC, therefore the trap effects may be ignored. Plugging in the linearized wavefunction into equation (B.1) gives

$$i\hbar\frac{\partial}{\partial t}\psi_0(1 + \nu) = \left[-\frac{\hbar^2}{2m}\nabla^2 + (U_0 + U_1\sin(\omega t))|\psi_0(1 + \nu)|^2 - U_0 n_0\right]\psi_0(1 + \nu). \tag{B.2}$$

The term on left hand side is

$$\begin{aligned}
i\hbar\frac{\partial}{\partial t}\psi_0(1 + \nu) &= i\hbar\frac{\partial\psi_0}{\partial t}(1 + \nu) + i\hbar\psi_0\frac{\partial(1 + \nu)}{\partial t} \\
&= i\hbar(\frac{-iU_1 n_0\sin(\omega t)}{\hbar})(1 + \nu)\psi_0 + i\hbar\frac{\partial\nu}{\partial t}\psi_0 \\
&= n_0 U_1\sin(\omega t)(1 + \nu)\psi_0 + i\hbar\frac{\partial\nu}{\partial t}\psi_0
\end{aligned} \tag{B.3}$$

The first term on the right hand side is

$$-\frac{\hbar^2}{2m}\psi_0\nabla^2(1 + \nu) = \frac{\hbar^2 k^2}{2m}\nu\psi_0 \tag{B.4}$$

The second term on the right hand side is

$$\begin{aligned}
&= (U_0 + U_1\sin(\omega t))|\psi_0(1 + \nu)|^2\psi_0(1 + \nu) \\
&= (U_0 + U_1\sin(\omega t))\psi_0\psi_0^*(1 + \nu)(1 + \nu^*)\psi_0(1 + \nu) \\
&= n_0(U_0 + U_1\sin(\omega t))(1 + \nu)(1 + \nu^*)(1 + \nu)\psi_0 \\
&= n_0(U_0 + U_1\sin(\omega t))(1 + \nu^* + 2\nu + 2\nu\nu^* + \nu^2 + \nu^2\nu^*)\psi_0 \\
&\approx n_0(U_0 + U_1\sin(\omega t))(1 + \nu^* + 2\nu)\psi_0
\end{aligned} \tag{B.5}$$

where for the last approximation the fact that $|\nu|^2 << 1$. The third term on the right hand side is

$$= U_0 n_0 \psi_0 (1 + \nu) \tag{B.6}$$

Combining the left hand side and the right hand side give

$$n_0 U_1 \sin(\omega t)(1+\nu)\psi_0 + i\hbar \frac{\partial \nu}{\partial t}\psi_0 = \frac{\hbar^2 k^2}{2m}\psi_0 \nu + n_0(U_0 + U_1 \sin(\omega t))(1 + \nu^* + 2\nu)\psi_0 - U_0 n_0 \psi_0(1+\nu)$$

$$\implies i\hbar \frac{\partial \nu}{\partial t} = \frac{\hbar^2 k^2}{2m}\nu + n_0(U_0 + U_1 \sin(\omega t))(\nu^* + \nu). \tag{B.7}$$

Since $\nu = (\xi + i\zeta)\cos(k \cdot r + \psi)$ we take the real and imaginary part of equation (B.7) giving

$$\Re : -\hbar\dot{\zeta} = \frac{\hbar^2 k^2}{2m}\xi + 2n_0(U_0 + U_1 \sin(\omega t))\xi. \tag{B.8}$$

By introducing constants $\Omega^2 = \frac{\hbar^2 k^4}{4m^2} + \frac{k^2 n_0 U_0}{m}$ and $\alpha = \frac{k^2 n_0 U_1}{m\Omega^2}$ equation (B.8) can be rewritten as

$$\dot{\zeta} = -\frac{2m}{\hbar k^2}\Omega^2 \left(1 + \alpha\sin(\omega t)\right)\xi \tag{B.9}$$

The imaginary part of equation (B.7) is

$$\Im : \hbar\dot{\xi} = \frac{\hbar^2 k^2}{2m}\zeta \tag{B.10}$$

Taking the time derivative of equation (B.10) gives

$$\ddot{\xi} = \frac{\hbar k^2}{2m}\dot{\zeta} \overset{1}{=} -\Omega^2 \left(1 + \alpha\sin(\omega t)\right)\xi. \tag{B.11}$$

which is equation (2.29). Taking the second time derivative of equation (B.8) gives

$$\ddot{\zeta} = -\frac{2n_0 U_1}{\hbar}\omega\cos(\omega t)\xi + \left(-\frac{\hbar^2 k^2}{2m} - 2n_0(U_0 + U_1\sin(\omega t))\right)\dot{\xi}.$$

Substituting equations (B.8) and (B.10) into the above equation gives

$$\ddot{\zeta} = \frac{\alpha\omega\cos(\omega t)}{1 + \alpha\sin(\omega t)}\dot{\zeta} - \Omega^2(1 + \alpha\sin(\omega t))\zeta. \tag{B.12}$$

which is equation (2.30)

Appendix C

Making the GPe dimensionless

Computers have a hard time dealing with small numbers such as $\hbar$ and m. Therefore the GPe equation (C.2) is made unitless. The following scheme is used in this thesis:

$$\Psi = \Psi_0 \tilde{\Psi}$$
$$\vec{r} = x_0 \tilde{\vec{r}} \tag{C.1}$$
$$t = t_0 \tilde{t}$$

where Ψ_0, x_0 and t_0 are constants with units 1/m, m and s respectively. The variables $\tilde{\Psi}$, $\tilde{\vec{r}}$ and $\tilde{t}$ are unitless. To find the relations between Ψ_0, x_0 and t_0 substitute equation (C.1) in GPe equation (C.2) giving:

$$i\frac{\partial \tilde{\Psi}}{\partial \tilde{t}} = \left[-\frac{\hbar}{2m}\frac{t_0}{x_0^2}\nabla^2 + \frac{t_0}{\hbar}V(\vec{r}) + \frac{t_0}{\hbar}\left(U_0 + U_1\sin(\omega t_0 \tilde{t})\right)|\Psi_0\tilde{\Psi}|^2 - \frac{t_0}{\hbar}U_0 n_0 \right]\tilde{\Psi} \tag{C.2}$$

Since we have a finite well of inner radius 13 μm the constant x_0 is set to $x_0 = 13$ μm. Then choosing

$$-\frac{\hbar}{2m}\frac{t_0}{x_0^2}\nabla^2 = -\frac{1}{2}\nabla^2 \implies t_0 = \frac{x_0^2}{\hbar}.$$

There are several ways to choose Ψ_0. The one used in this thesis starts by considering the norm of Ψ which is $\int dr|\Psi|^2 = N$. This means

$$N = \int dr|\Psi|^2 = x_0^2\Psi_0^2\int d\tilde{r}|\tilde{\Psi}|^2$$
$$= x_0^2\Psi_0^2\tilde{N}.$$

In this thesis $\tilde{N}$ is set to equal one giving $\Psi_0 = \sqrt{N}/x_0$. Then the following GPe equation is obtained

$$i\frac{\partial \tilde{\Psi}}{\partial \tilde{t}} = \left[-\frac{1}{2}\nabla^2 + \frac{t_0}{\hbar}V(\vec{r}) + \left(\frac{t_0}{\hbar}\Psi_0^2 U_0 + \frac{t_0}{\hbar}\Psi_0^2 U_1\sin(\omega t_0 \tilde{t})\right)|\tilde{\Psi}|^2 - \frac{t_0}{\hbar}U_0 n_0 \right]\tilde{\Psi}. \tag{C.3}$$

where the parameters can be redefined as $\tilde{V} = t_0/\hbar V(\vec{r})$, $\tilde{U}_0 = \frac{t_0}{\hbar}\Psi_0^2 U_0$, $\tilde{U}_1 = \frac{t_0}{\hbar}\Psi_0^2 U_1$, $\tilde{\omega} = t_0\omega$ and $\tilde{n} = \frac{t_0}{\hbar}U_0 n_0$. Equation (C.3) is exclusively used for numeric simulations in this thesis.

The physical parameters of the problems were defined in section 2.4.3. Their unitless form have the following values

$$\tilde{N} = 1$$
$$\tilde{R}_{\text{in}} = 1$$
$$\tilde{R}_{\text{out}} = 1.5\tilde{R}_{\text{in}}$$
$$\tilde{V} = 444.4394405$$
$$\tilde{U}_0 = 28.7915428$$
$$\tilde{U}_1 = 287.915428$$
$$\tilde{\omega} = 1377.7622648$$
$$\tilde{n} = 15.65038$$

(C.4)

for the case of the circle. For the other three trap shapes all the values, except for $\tilde{R}_{\text{in}}$ and $\tilde{R}_{\text{out}}$, in equation (C.4) remain the same. For $\tilde{R}_{\text{in}}$ the value is chosen such that all the areas of the different trap geometries are $A = \pi$.